

# Lawrence Berkeley National Laboratory

## LBL Publications

### Title

Involvement of 5f Orbitals in the Covalent Bonding between the Uranyl Ion and Trialkyl Phosphine Oxide: Unraveled by Oxygen K-Edge X-ray Absorption Spectroscopy and Density Functional Theory

### Permalink

<https://escholarship.org/uc/item/6s3220bz>

### Journal

Inorganic Chemistry, 61(1)

### ISSN

0020-1669

### Authors

Zhang, Yusheng

Duan, Wuhua

Yang, Yuning

et al.

### Publication Date

2022-01-10

### DOI

10.1021/acs.inorgchem.1c02236

Peer reviewed

# Involvement of 5f Orbitals in the Covalent Bonding between the Uranyl Ion and Trialkyl Phosphine Oxide: Unraveled by Oxygen K-Edge X-ray Absorption Spectroscopy and Density Functional Theory

Yusheng Zhang, Wuhua Duan, Yuning Yang, Tian Jian, Yusen Qiao, Guoxi Ren, Nian Zhang, Lei Zheng, Wensheng Yan, Jianchen Wang, Jing Chen, Stefan G. Minasian, and Taoxiang Sun\*



Cite This: <https://doi.org/10.1021/acs.inorgchem.1c02236>



Read Online

ACCESS |



Metrics & More



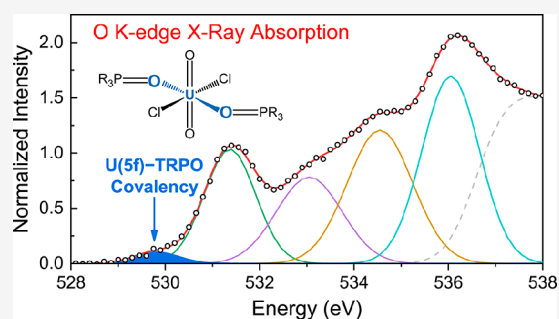
Article Recommendations



Supporting Information

**ABSTRACT:** Monodentate organophosphorus ligands have been used for the extraction of the uranyl ion ( $\text{UO}_2^{2+}$ ) for over half a century and have exhibited exceptional extractability and selectivity toward the uranyl ion due to the presence of the phosphoryl group ( $\text{O}=\text{P}$ ). Tributyl phosphate (TBP) is the extractant of the world-renowned PUREX process, which selectively recovers uranium from spent nuclear fuel. Trialkyl phosphine oxide (TRPO) shows extractability toward the uranyl ion that far exceeds that for other metal ions, and it has been used in the TRPO process. To date, however, the mechanism of the high affinity of the phosphoryl group for  $\text{UO}_2^{2+}$  remains elusive. We herein investigate the bonding covalency in a series of complexes of  $\text{UO}_2^{2+}$  with TRPO by oxygen K-edge X-ray absorption spectroscopy (XAS) in combination with density functional theory (DFT) calculations.

Four TRPO ligands with different R substituents are examined in this work, for which both the ligands and their uranyl complexes are crystallized and investigated. The study of the electronic structure of the TRPO ligands reveals that the two TRPO molecules, irrespective of their substituents, can engage in  $\sigma$ - and  $\pi$ -type interactions with U 5f and 6d orbitals in the  $\text{UO}_2\text{Cl}_2(\text{TRPO})_2$  complexes. Although both the axial ( $\text{O}_{\text{ax}}$ ) and equatorial ( $\text{O}_{\text{eq}}$ ) oxygen atoms in the  $\text{UO}_2\text{Cl}_2(\text{TRPO})_2$  complexes contribute to the X-ray absorption, the first pre-edge feature in the O K-edge XAS with a small intensity is exclusively contributed by  $\text{O}_{\text{eq}}$  and is assigned to the transition from  $\text{O}_{\text{eq}}$  1s orbitals to the unoccupied molecular orbitals of  $1b_{1u} + 1b_{2u} + 1b_{3u}$  symmetries resulting from the  $\sigma$ - and  $\pi$ -type mixing between U 5f and  $\text{O}_{\text{eq}}$  2p orbitals. The small intensity in the experimental spectra is consistent with the small amount of  $\text{O}_{\text{eq}}$  2p character in these orbitals for the four  $\text{UO}_2\text{Cl}_2(\text{TRPO})_2$  complexes as obtained by Mulliken population analysis. The DFT calculations demonstrate that the U 6d orbitals are also involved in the U–TRPO bonding interactions in the  $\text{UO}_2\text{Cl}_2(\text{TRPO})_2$  complexes. The covalent bonding interactions between TRPO and  $\text{UO}_2^{2+}$ , especially the contributions from U 5f orbitals, while appearing to be small, are sufficiently responsible for the exceptional extractability and selectivity of monodentate organophosphorus ligands for the uranyl ion. Our results provide valuable insight into the fundamental actinide chemistry and are expected to directly guide actinide separation schemes needed for the development of advanced nuclear fuel cycle technologies.



## INTRODUCTION

Extraction separation of the uranyl ion ( $\text{UO}_2^{2+}$ ) is of great significance for the efficient utilization of uranium resources and thus the sustainable development of nuclear energy.<sup>1–4</sup> A number of ligands have been adopted for the extraction of  $\text{UO}_2^{2+}$ , among which the monodentate organophosphorus extractants display prominent extractability and selectivity.<sup>1,5</sup> For example, tributyl phosphate (TBP) is the extractant of the world-renowned PUREX process to recover  $\text{UO}_2^{2+}$  from spent nuclear fuel.<sup>1</sup> Another example is trialkyl phosphine oxide (TRPO), which shows higher extractability for  $\text{UO}_2^{2+}$  than does TBP. The TRPO ligands are used as extractants in the TRPO process, recovering the uranyl ion and other actinides from high-level liquid waste.<sup>6</sup> In the TRPO process, the

distribution ratio of  $\text{UO}_2^{2+}$  far exceeds that for other metal ions.<sup>6</sup> The interactions of the phosphoryl group ( $\text{O}=\text{P}$ ) in these ligands with  $\text{UO}_2^{2+}$  are considered to be responsible for the extraordinary extractability and selectivity and have been investigated by crystallography and theoretical calculations over the past several decades.<sup>7–18</sup> The crystal structures suggest the coordination of the oxygen atoms in the

Received: July 26, 2021



ACS Publications

© XXXX American Chemical Society

A

<https://doi.org/10.1021/acs.inorgchem.1c02236>  
Inorg. Chem. XXXX, XXX, XXX–XXX

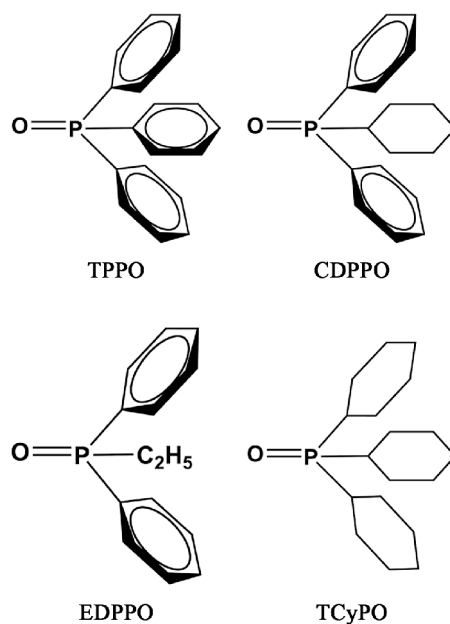
53 phosphoryl group with  $\text{UO}_2^{2+}$ . The theoretical calculations  
54 provide the geometry of the complexes and the binding  
55 energies between TRPO and  $\text{UO}_2^{2+}$ , and the bonding order  
56 analysis indicates the ionic bonding properties between  $\text{UO}_2^{2+}$   
57 and the phosphoryl group.<sup>16–18</sup> These studies are, however,  
58 insufficient to account for the high extractability and selectivity  
59 of the monodentate organophosphorus extractants for  $\text{UO}_2^{2+}$ ,  
60 and its underlying mechanism requires further investigation.

61 The most significant character that distinguishes uranium  
62 from transition metals and lanthanides is the presence of 5f and  
63 6d orbitals. The involvement of both 5f and 6d orbitals in the  
64 covalent bonds between uranium and axial oxygen ( $\text{O}_{\text{yl}}$ ) atoms  
65 induces a geometrically linear and redox-stable uranyl ion,<sup>19–22</sup>  
66 around which other ligands are confined to the equatorial  
67 plane. Exploring the coordination behavior between the uranyl  
68 ion and the equatorial ligands is an essential issue of current  
69 interest because of the direct relevance to the extraction  
70 behavior of extractants.<sup>23–26</sup> Indications are gradually emerg-  
71 ing that the selectivity of extractants toward specific metal ions  
72 is related to their covalent bonding interactions.<sup>27,28</sup> Given the  
73 great involvement of the U 5f orbitals in chemical bonding,<sup>20,21</sup>  
74 we hypothesized that covalency in the bonding interaction  
75 between the uranyl ion and the O-donor from the phosphoryl  
76 group,  $\text{U}-(\text{O}=\text{P})$ , may be partially responsible for the  
77 remarkable extractability and selectivity of the monodentate  
78 organophosphorus extractants for the uranyl ion.

79 As one of the most versatile and direct spectroscopic  
80 techniques in the evaluation of the bonding covalency in d and  
81 f block compounds, ligand K-edge X-ray absorption spectroscopy  
82 (XAS) in combination with density functional theory  
83 (DFT) and time-dependent DFT (TDDFT) calculations have  
84 attracted much attention in the past decades.<sup>29–47</sup> The ligand  
85 K-edge XAS probes the transition from the ligand 1s orbitals to  
86 unoccupied molecular orbitals (MOs) containing ligand p  
87 character. This technique can quantify the component of  
88 ligand p character in the metal d and f orbitals, hence the  
89 covalency of the metal–ligand bond.<sup>29</sup> To guide the  
90 interpretation of the XAS spectra, DFT can manifest the  
91 orbital energy levels and orbital compositions, which are  
92 related to the transition energies and intensities, respectively.  
93 TDDFT can simulate the XAS spectra to compare with the  
94 experimental spectra. XAS and DFT/TDDFT in combination  
95 have been implemented to reveal the covalent bonding  
96 behavior of the f and d orbitals of lanthanides and actinides  
97 upon mixing with p orbitals of ligands.<sup>33–47</sup>

98 Our goal in this work is to provide insight into the  
99 contributions of U 6d and especially 5f orbitals to chemical  
100 bonding covalency between  $\text{UO}_2^{2+}$  and phosphoryl group,  
101 thereby revealing the mechanism of the remarkable extract-  
102 ability and selectivity of the monodentate organophosphorus  
103 extractants for  $\text{UO}_2^{2+}$ . Complexes of TBP and  $\text{UO}_2^{2+}$  cannot  
104 be isolated as pure crystalline materials with high symmetry  
105 that is desirable for spectroscopic analysis.<sup>48–50</sup> To overcome  
106 this challenge, we have tested four different TRPO ligands  
107 (Scheme 1), and obtained the single crystals of both the  
108 ligands and the uranyl complexes, including triphenyl  
109 phosphine oxide (TPPO), cyclohexyldiphenyl phosphine  
110 oxide (CDPPO), ethyldiphenyl phosphine oxide (EDPPO),  
111 and tricyclohexyl phosphine oxide (TCyPO). These four  
112 ligands have demonstrated excellent extraction and separation  
113 performance toward the uranyl ion (Figure S1). Elementary  
114 covalent interactions between  $\text{UO}_2^{2+}$  and TRPO in the entire  
115 series of  $\text{UO}_2\text{Cl}_2(\text{TRPO})_2$  complexes are examined using

Scheme 1. Molecular Structures of the Ligands Used in the Present Work



oxygen K-edge XAS, with the interpretation guided by DFT/  
TDDFT calculations. This allows us to examine the electronic  
structures of both the TRPO ligands and the  $\text{UO}_2\text{Cl}_2(\text{TRPO})_2$   
complexes as well as the effect of the R substituents of the  
TRPO ligands on their interactions with the uranyl ion.

## RESULTS AND DISCUSSION

**Sample Preparation.** All the TRPO and  $\text{UO}_2\text{Cl}_2(\text{TRPO})_2$   
complexes studied in this work were prepared in large  
quantities, isolated as highly pure crystalline solids, and  
characterized by single-crystal X-ray diffraction prior to  
use.<sup>7–13,51–59</sup> Chloride is employed as the counterion in the  
 $\text{UO}_2\text{Cl}_2(\text{TRPO})_2$  complexes to avoid the interference of the  
oxygen-containing anions such as nitrate to the O K-edge XAS  
spectra. All the crystal structures of TRPO and  
 $\text{UO}_2\text{Cl}_2(\text{TRPO})_2$  obtained in this work are illustrated in  
Figure 1. Data collection and refinement details are available in  
Tables S1 and S2. Some of the TRPO ligands and  
 $\text{UO}_2\text{Cl}_2(\text{TRPO})_2$  complexes have been reported previ-  
ously;<sup>7–13,51–59</sup> however, to the best of our knowledge, the  
crystal structures of CDPPO,  $\text{UO}_2\text{Cl}_2(\text{CDPPO})_2$ , and  
 $\text{UO}_2\text{Cl}_2(\text{EDPPO})_2$  have not been reported. The  $\text{P}=\text{O}$  bond  
length varies from 1.487 to 1.493 Å in TRPO (Table S3), and  
these values increase to about 1.519 Å in the  $\text{UO}_2\text{Cl}_2(\text{TRPO})_2$   
complexes (Table S4), suggesting the bonding interaction  
between the TRPO ligands and the uranyl ion. The two TRPO  
ligands are trans to each other in all the  $\text{UO}_2\text{Cl}_2(\text{TRPO})_2$   
complexes, maintaining the complexes in  $C_i$  symmetry. The  
 $\text{U}-\text{O}_{\text{eq}}$  bond length is in the range of 2.288–2.307 Å, much  
longer than the  $\text{U}-\text{O}_{\text{yl}}$  bond length (1.762–1.769 Å). The  
distances between uranium and axial oxygen ( $\text{O}_{\text{yl}}$ ) as well as  
those between uranium and the oxygen of TRPO in the  
equatorial plane ( $\text{O}_{\text{eq}}$ ) show no apparent difference in the four  
 $\text{UO}_2\text{Cl}_2(\text{TRPO})_2$  complexes. On the basis of this analysis of  
the geometric data obtained by X-ray crystallography, changing  
the substituents in TRPO has no evident effect on the bonding  
interaction with the uranyl ion.

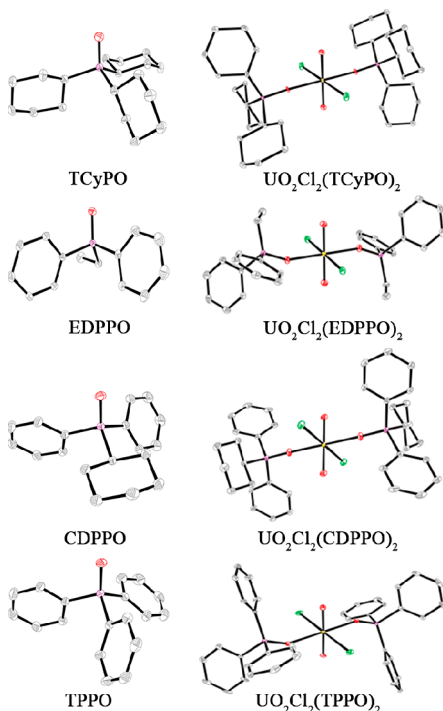


**Figure 1.** Crystal structures of TRPO and  $\text{UO}_2\text{Cl}_2(\text{TRPO})_2$  investigated in this work with thermal ellipsoids drawn at the 30% probability level. Hydrogen atoms have been omitted for clarity. Oxygen, phosphorus, carbon, chloride, and uranium atoms are in red, purple, white, green, and yellow, respectively.

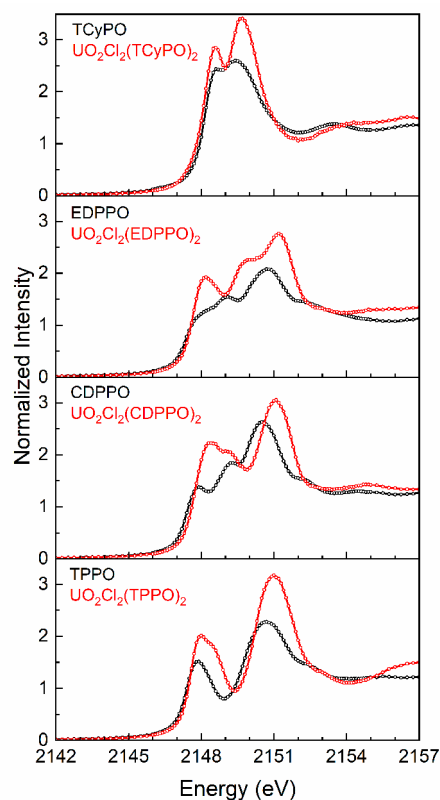


**Figure 2.** Background-subtracted and normalized P K-edge XAS spectra for the free ligands TRPO (black) and their uranyl complexes  $\text{UO}_2\text{Cl}_2(\text{TRPO})_2$  (red).

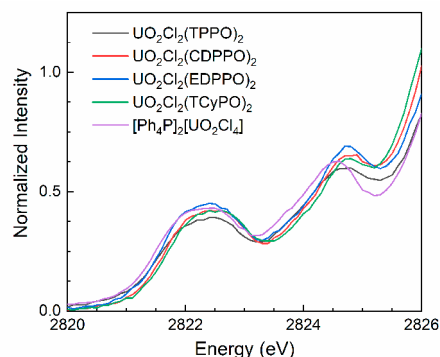


**Figure 3.** Background-subtracted and normalized Cl K-edge XAS spectra for the  $\text{UO}_2\text{Cl}_2(\text{TRPO})_2$  complexes in comparison with that for  $[\text{Ph}_4\text{P}]_2[\text{UO}_2\text{Cl}_4]$ . For curve-fitting analysis, refer to Figure S6.

Cl 3p orbitals with the U 5f and 6d orbitals are not significantly perturbed when varying the other equatorial ligands.

**O K-edge XAS.** Since the P and Cl K-edge XAS measurements only provided indirect probes of the U–O bonds, we sought additional insights using O K-edge XAS. The O K-edge XAS data were collected by total fluorescence yield (TFY) detection for both TRPO and the  $\text{UO}_2\text{Cl}_2(\text{TRPO})_2$  complexes. The background-subtracted and normalized O K-edge XAS are shown in Figure 4. In the TRPO series, the pre-edge features show substantial differences with the variation of the R substituents. A substantial pre-edge transition around 532 eV is observed in the spectrum of TPPO, which is diminished in the spectra of CDPPO and EDPPPO. For

**P and Cl K-Edge XAS.** Spectra at the P and Cl K-edges were measured initially to probe electronic structure from the perspective of heavier atoms in the coordination sphere. Previous studies have shown that P or Cl K-edge XAS can be sensitive to bonding with phosphine or chloride ligands directly bound to metal centers.<sup>33–39,60–65</sup> Figure 2 shows the background-subtracted and normalized P K-edge XAS spectra for the free ligands TRPO and their uranyl complexes  $\text{UO}_2\text{Cl}_2(\text{TRPO})_2$ . In the P K-edge XAS of the TRPO series, the pre-edge features show substantial differences with the variation of the R substituents. A pre-edge feature around 2147.8 eV is observed in the spectrum of TPPO, CDPPO, and EDPPPO, and this feature disappears in the spectrum of TCyPO. Peak shift and transition intensity variations are observed when comparing the P K-edge XAS of  $\text{UO}_2\text{Cl}_2(\text{TRPO})_2$  with that of TRPO, indicating the change of the electron distribution on the phosphorus atoms, and thus the bonding interaction between TRPO and the uranyl ion in the  $\text{UO}_2\text{Cl}_2(\text{TRPO})_2$  complexes.

Spectra at the Cl K-edge were measured to probe changes in electronic structure from the perspective of the chloride ligands in the  $\text{UO}_2\text{Cl}_2(\text{TRPO})_2$  complexes (Figure 3). The spectra are similar to that previously reported for  $[\text{Ph}_4\text{P}]_2[\text{UO}_2\text{Cl}_4]$ ,<sup>37</sup> in that closely spaced pre-edge features are observed at 2822.4 and 2824.8 eV for all complexes. Previous DFT analyses for  $[\text{Ph}_4\text{P}]_2[\text{UO}_2\text{Cl}_4]$  indicated that these features arise from transitions between the Cl 1s orbitals to the unoccupied MOs of  $1b_{1u} + 1b_{2u} + 1b_{3u} + 2b_{2u}$  and  $1b_{1g}$  symmetries, respectively.<sup>37</sup> The close correspondence between the Cl K-edge spectra for  $[\text{Ph}_4\text{P}]_2[\text{UO}_2\text{Cl}_4]$  and each of the  $\text{UO}_2\text{Cl}_2(\text{TRPO})_2$  complexes indicates that the interactions of

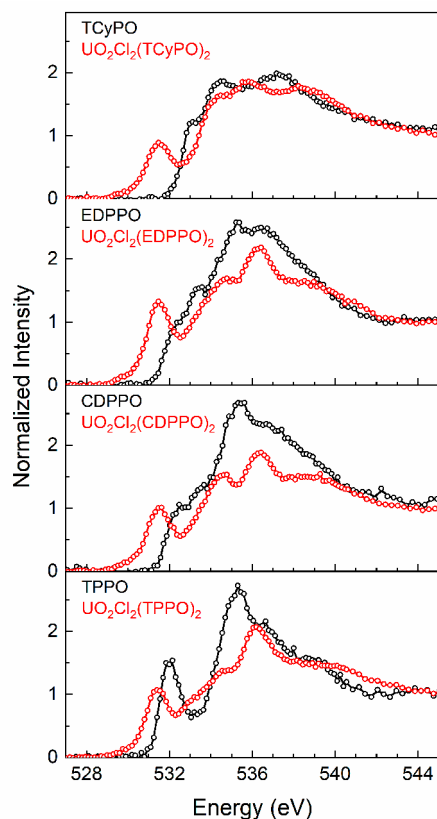


**Figure 4.** Background-subtracted and normalized O K-edge XAS spectra for the free ligands TRPO (black) and their uranyl complexes  $\text{UO}_2\text{Cl}_2(\text{TRPO})_2$  (red).

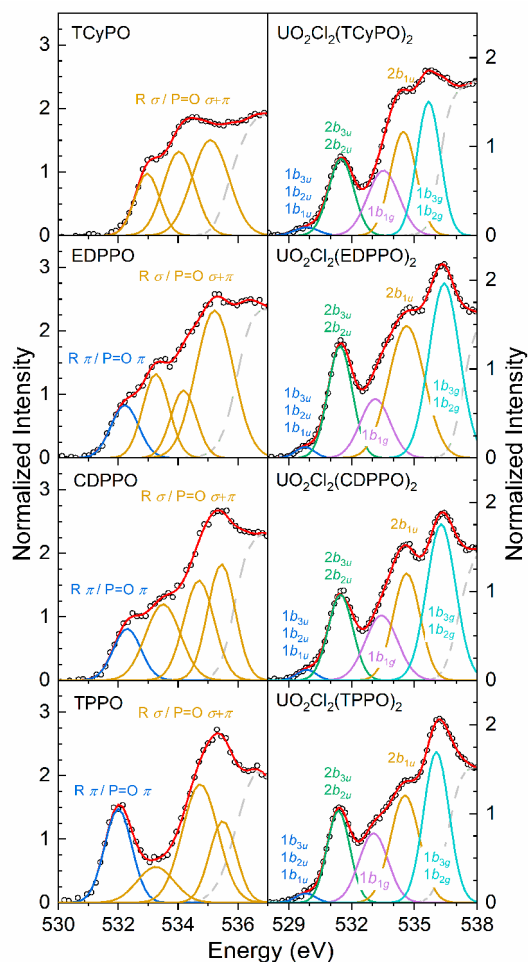


**Figure 5.** Curve-fitting results for O K-edge XAS for TRPO (left) and  $\text{UO}_2\text{Cl}_2(\text{TRPO})_2$  (right). The experimental data are shown in black circles, and the total curve fits are shown in red traces. Postedge residuals (dashed gray traces) are generated by subtracting the pre-edge Gaussian functions (blue, yellow, green, purple, and light blue) from the total curve fits.

196 TCyPO, no transition at 532 eV is observed in the O K-edge  
197 XAS. All the  $\text{UO}_2\text{Cl}_2(\text{TRPO})_2$  complexes display similar pre-  
198 edge features in the O K-edge spectra, with a distinct pre-edge  
199 feature near 531.5 eV and a small shoulder feature around 530  
200 eV. One can see from Figure 4 that the onset of the pre-edge  
201 XAS for all the  $\text{UO}_2\text{Cl}_2(\text{TRPO})_2$  complexes moves to lower  
202 energy as compared with that of TRPO, locating around 530  
203 eV. The difference in the O K-edge XAS between TRPO and  
204  $\text{UO}_2\text{Cl}_2(\text{TRPO})_2$  is supposed to be a result of two factors. One  
205 is that the only oxygen in TRPO is from the O=P moiety,  
206 whereas in the  $\text{UO}_2\text{Cl}_2(\text{TRPO})_2$  complexes, both the  
207 equatorial and axial oxygen atoms contribute to the pre-edge  
208 transitions. The other one is the covalent interaction between  
209 the uranyl ion and TRPO, which has been confirmed by the  
210 peak shift and intensity variation in comparing the P K-edge  
211 XAS for TRPO and  $\text{UO}_2\text{Cl}_2(\text{TRPO})_2$  in Figure 2.

212 The O K-edge XAS spectra of both TRPO and  
213  $\text{UO}_2\text{Cl}_2(\text{TRPO})_2$  were modeled with Gaussian functions and  
214 a step function using an error function to identify the exact  
215 energy of the pre-edge features as well as to quantify the  
216 intensities. The energy positions of the peaks are determined  
217 by the second derivatives and are fixed during the curve fits  
218 (Figures S2 and S4). Other fitting parameters, including the  
219 peak amplitude and the half width, are entirely unconstrained.  
220 Figure 5 shows the modeling results for the pre-edge regions of  
221 the spectra for TRPO and  $\text{UO}_2\text{Cl}_2(\text{TRPO})_2$ , and the complete  
222 fits and fitting parameters are provided in Figures S3 and S5  
223 and Tables S5 and S6).

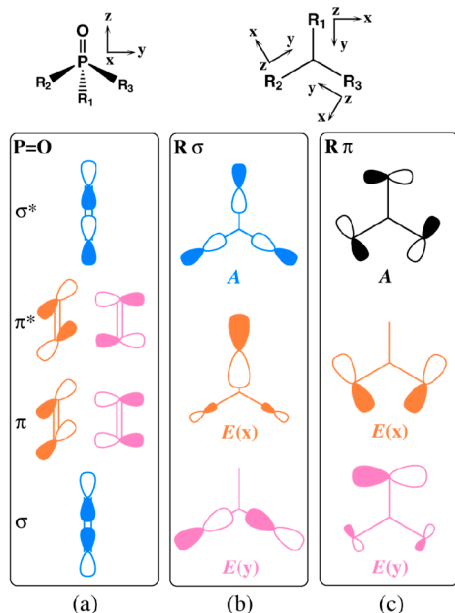
224 In the TRPO series, the best fits of the spectra for TPPO,  
225 CDPPO, and EDPPO are acquired using four pre-edge

features from 531 to 537 eV. In contrast, using only three  
pre-edge features at 533.0, 534.0, and 535.1 eV can give a high-  
quality curve fit of the spectrum for TCyPO. For the  
 $\text{UO}_2\text{Cl}_2(\text{TRPO})_2$  complexes, all the spectra are adequately  
modeled by five resolved pre-edge features. Table 1  
summarizes the transition energies and intensities in modeling  
the O K-edge XAS for  $\text{UO}_2\text{Cl}_2(\text{TRPO})_2$ . All the spectra of  
 $\text{UO}_2\text{Cl}_2(\text{TRPO})_2$  reveal similar transition energies and  
intensities in the pre-edge regions, containing a low-intensity  
pre-edge shoulder at 529.8 eV, an intermediate-intensity pre-  
edge feature around 533.1 eV, and three high-intensity pre-  
edge features near 531.4, 534.6, and 536.0 eV.

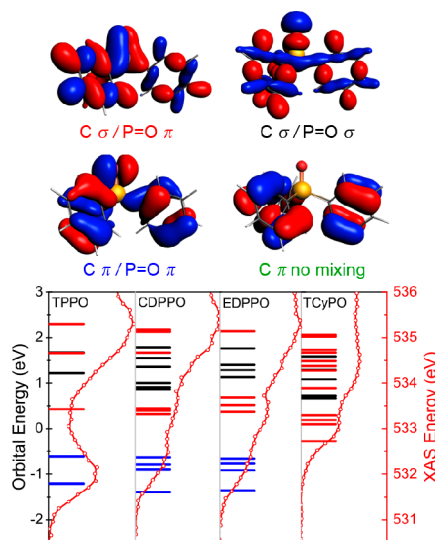
**Ground-State Electronic Structure of TRPO.** The  
electronic structure of TRPO is investigated to clarify its  
orbitals that can interact with the uranyl ion and to provide a  
basis for interpreting the above O K-edge XAS of TRPO. In  
the O=P moiety of TRPO, the O 2p orbitals can mix with P  
3p orbitals to form both  $\sigma$ - and  $\pi$ -bonds, as shown in Scheme  
2, and the fragment orbitals of P=O can mix with the  
symmetry-adapted linear combinations (SALCs) of the orbitals  
from the three R substituents. Taking  $C_3$ -symmetric TPPO as  
an example, the three phenyl substitutions of TPPO provide

**Table 1. Energy and Intensity Obtained by Curve-Fitting of the O K-edge XAS for  $\text{UO}_2\text{Cl}_2(\text{TRPO})_2$** 

transition	curve fitting	
	energy (eV)	intensity
$\text{UO}_2\text{Cl}_2(\text{TPPO})_2$		
$1s \rightarrow 1b_{1u} + 1b_{2u} + 1b_{3u}$	529.8	0.12
$1s \rightarrow 2b_{2u} + 2b_{3u}$	531.4	1.41
$1s \rightarrow 1b_{1g}$	533.0	1.36
$1s \rightarrow 2b_{1u}$	534.6	2.10
$1s \rightarrow 1b_{2g} + 1b_{3g}$	536.0	2.58
$\text{UO}_2\text{Cl}_2(\text{CDPPO})_2$		
$1s \rightarrow 1b_{1u} + 1b_{2u} + 1b_{3u}$	529.8	0.14
$1s \rightarrow 2b_{2u} + 2b_{3u}$	531.5	1.43
$1s \rightarrow 1b_{1g}$	533.4	1.42
$1s \rightarrow 2b_{1u}$	534.6	1.95
$1s \rightarrow 1b_{2g} + 1b_{3g}$	536.3	3.04
$\text{UO}_2\text{Cl}_2(\text{EDPPO})_2$		
$1s \rightarrow 1b_{1u} + 1b_{2u} + 1b_{3u}$	529.8	0.14
$1s \rightarrow 2b_{2u} + 2b_{3u}$	531.4	1.83
$1s \rightarrow 1b_{1g}$	533.1	1.19
$1s \rightarrow 2b_{1u}$	534.6	3.19
$1s \rightarrow 1b_{2g} + 1b_{3g}$	536.4	3.59
$\text{UO}_2\text{Cl}_2(\text{TCyPO})_2$		
$1s \rightarrow 1b_{1u} + 1b_{2u} + 1b_{3u}$	529.8	0.13
$1s \rightarrow 2b_{2u} + 2b_{3u}$	531.5	1.31
$1s \rightarrow 1b_{1g}$	533.5	1.38
$1s \rightarrow 2b_{1u}$	534.5	1.82
$1s \rightarrow 1b_{2g} + 1b_{3g}$	535.7	2.11

**Scheme 2. Qualitative MOs Correlation Diagram of TRPO in  $C_3$  Point Group Symmetry**

The bonding interactions within the TRPO molecules are confirmed by ground-state DFT calculations. Four canonical Kohn–Sham orbitals of TPPO calculated at the B3LYP/TZ2P level are illustrated in Figure 6. The truncated unoccupied

**Figure 6. Contours of the representative MOs (0.03 au) for TPPO (top), and comparisons of the calculated MOs energy levels with the experimental O K-edge XAS for TRPO (bottom).**

MOs energy level diagram for TRPO, which has been shifted by a constant to make the energies of O 1s orbitals equivalent to each other for comparison with the O K-edge XAS, is also presented in Figure 6. For the ligands TPPO, CDPPO, and EDPPO, there are orbitals belonging to the phenyl  $\pi$ -orbitals mixing with O=P  $\pi$ -orbitals between  $-1.5$  and  $0.5$  eV. In contrast, TCyPO has no R  $\pi$ /P=O  $\pi$ -type MOs due to the lack of phenyl rings and therefore has no orbitals in this region. This difference is in perfect agreement with the experimental O K-edge XAS, where the transitions around 532 eV in the spectra for TPPO, CDPPO, and EDPPO are not observed in that for TCyPO. The remaining peaks at the region from 533 to 536 eV in the O K-edge XAS for all the TRPO complexes are attributed to the electronic transitions from O 1s orbitals to the unoccupied MOs formed by the mixing of R  $\sigma$ -orbitals with O=P ( $\pi + \sigma$ )-orbitals.

The group theory analysis and DFT calculations reveal that the TRPO ligands can provide both  $\sigma$ - and  $\pi$ -orbitals to interact with the uranyl ion in the  $\text{UO}_2\text{Cl}_2(\text{TRPO})_2$  complexes since oxygen in the O=P group can be both a  $\sigma$ - and  $\pi$ -donor. The hybridization of the O=P fragment orbitals depends on the type of the substituents in TRPO. The orbitals from phenyl rings can mix with the O=P fragment orbitals through both  $\sigma$ - and  $\pi$ -type bonding interactions, whereas the orbitals from alkyl substituents can only provide  $\sigma$ -orbitals to mix with the O=P fragment orbitals. Therefore, no transitions to R  $\pi$ /P=O  $\pi$  MOs are observed in the O K-edge XAS of TCyPO.

#### Ground-State Electronic Structure of $\text{UO}_2\text{Cl}_2(\text{TRPO})_2$

The chemical bonding interactions between uranyl moiety and TRPO ligands in  $\text{UO}_2\text{Cl}_2(\text{TRPO})_2$  are analyzed by group theory and DFT calculations, and the discussion will focus on the unoccupied orbitals most relevant to the O K-edge XAS experiments. In the O K-edge XAS of  $\text{UO}_2\text{Cl}_2(\text{TRPO})_2$ , both the  $\text{O}_{\text{eq}}$  and  $\text{O}_{\text{yl}}$  atoms contribute to the pre-edge transitions. The bonding interactions between U and  $\text{O}_{\text{yl}}$  have been widely

both  $\sigma$ - and  $\pi$ -type interactions with the O=P moiety. The  $\sigma$ -type SALCs of R orbitals span A and E symmetries to mix with the O=P  $\sigma$ - and  $\pi$ -type orbitals, respectively. The  $\pi$ -type SALCs of the R orbitals span A and E symmetries, whereas only those of E symmetry can mix with the O=P  $\pi$ -type orbitals. That of A symmetry cannot interact with the O=P  $\sigma$ - or  $\pi$ -type orbitals.

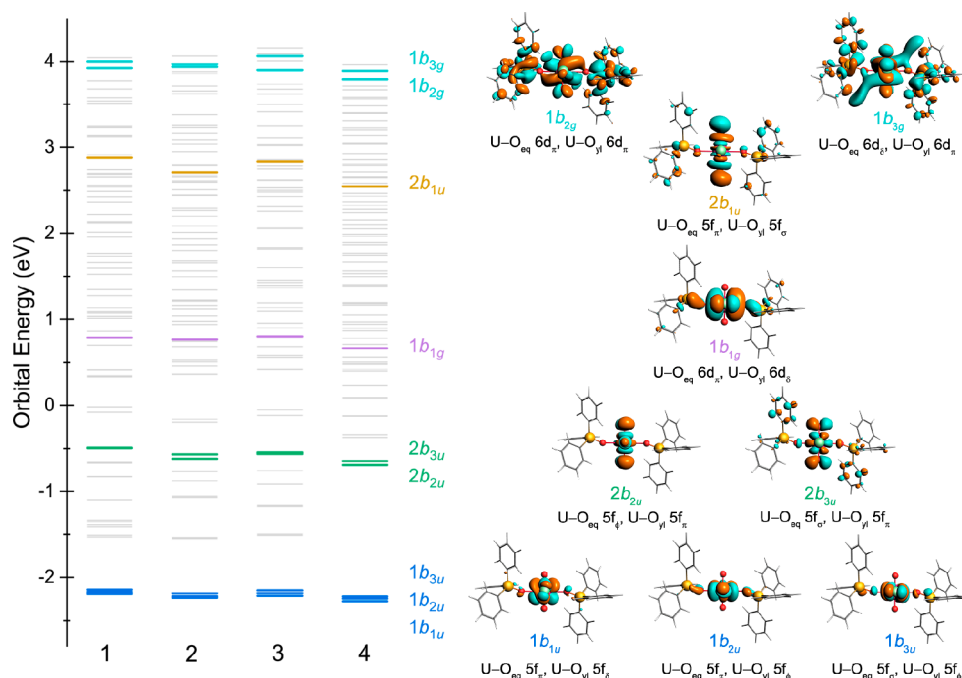


**Figure 7.** Truncated MOs energy levels for  $\text{UO}_2\text{Cl}_2(\text{TRPO})_2$  calculated at DFT/B3LYP level (left) and the contours of unoccupied Kohn–Sham orbitals (0.02 au) relevant to the orbital interactions between the uranyl ion and TRPO (right).

studied. The two axial U–O<sub>yl</sub> triple bonds are formed by mixing of U 5f and 6d orbitals with the O<sub>yl</sub> 2p orbitals, resulting in two  $\sigma$ - and four  $\pi$ -bonding orbitals ( $\sigma_u^2 \pi_u^4 \sigma_g^2 \pi_g^4$ ).<sup>19–21,66</sup> For the chemical bonding between the uranyl ion and the equatorial oxygen atoms from TRPO ligands, it is quite simplistic to perform group theory analysis on  $\text{UO}_2\text{Cl}_2(\text{TRPO})_2$  assuming  $D_{2h}$  symmetry by ignoring the phosphorus atom of TRPO and the substituents on it. The fragment orbitals provided by the two TRPO molecules can form four  $\pi$ -type SALCs spanning  $b_{1u} + b_{2u} + b_{1g} + b_{2g}$  symmetries and two  $\sigma$ -type SALCs spanning  $b_{3u} + a_g$  symmetries. The SALCs of  $b_{1u}$  and  $b_{2u}$  symmetries can mix with the U 5f orbitals to form  $\pi$  U–TRPO bonding interactions of  $1b_{1u}$  (U–O<sub>eq</sub> 5f <sub>$\pi$</sub> , U–O<sub>yl</sub> 5f <sub>$\delta$</sub> ),  $1b_{2u}$  (U–O<sub>eq</sub> 5f <sub>$\pi$</sub> , U–O<sub>yl</sub> 5f <sub>$\phi$</sub> ), and  $2b_{1u}$  (U–O<sub>eq</sub> 5f <sub>$\pi$</sub> , U–O<sub>yl</sub> 5f <sub>$\sigma$</sub> ) symmetries. The SALCs of  $b_{3u}$  symmetry can mix with the U 5f orbitals to form  $\sigma$  U–TRPO bonding interactions of  $1b_{3u}$  (U–O<sub>eq</sub> 5f <sub>$\sigma$</sub> , U–O<sub>yl</sub> 5f <sub>$\phi$</sub> ) and  $2b_{3u}$  (U–O<sub>eq</sub> 5f <sub>$\sigma$</sub> , U–O<sub>yl</sub> 5f <sub>$\pi$</sub> ) symmetries. This leaves the U 5f orbital of  $1a_u$  (U–O<sub>eq</sub> 5f <sub>$\delta$</sub> , U–O<sub>yl</sub> 5f <sub>$\delta$</sub> ) symmetry as nonbonding with respect to both O<sub>eq</sub> and O<sub>yl</sub> atoms and that of  $2b_{2u}$  (U–O<sub>eq</sub> 5f <sub>$\phi$</sub> , U–O<sub>yl</sub> 5f <sub>$\pi$</sub> ) symmetry as nonbonding with respect to O<sub>eq</sub> atoms and  $\pi$ -bonding with respect to O<sub>yl</sub> atoms. For the chemical bonding between TRPO and U 6d orbitals, the SALCs of  $b_{1g} + b_{2g}$  symmetries can mix with the U 6d orbitals to form  $\pi$  U–TRPO bonding interactions of  $1b_{1g}$  (U–O<sub>eq</sub> 6d <sub>$\pi$</sub> , U–O<sub>yl</sub> 6d <sub>$\delta$</sub> ) and  $1b_{2g}$  (U–O<sub>eq</sub> 6d <sub>$\pi$</sub> , U–O<sub>yl</sub> 6d <sub>$\pi$</sub> ) symmetries. The SALCs of  $a_g$  symmetries can mix with the U 6d orbitals to form  $\sigma$  U–TRPO bonding interactions of  $1a_g$  (U–O<sub>eq</sub> 6d <sub>$\sigma$</sub> , U–O<sub>yl</sub> 6d <sub>$\delta$</sub> ) and  $2a_g$  (U–O<sub>eq</sub> 6d <sub>$\sigma$</sub> , U–O<sub>yl</sub> 6d <sub>$\sigma$</sub> ) symmetries. This leaves the U 6d orbital of  $b_{3g}$  (U–O<sub>eq</sub> 6d <sub>$\delta$</sub> , U–O<sub>yl</sub> 6d <sub>$\pi$</sub> ) symmetry as nonbonding with respect to O<sub>eq</sub> atoms and  $\pi$ -bonding with respect to O<sub>yl</sub> atoms. Figure 7 shows the truncated energy levels of the unoccupied MOs of  $\text{UO}_2\text{Cl}_2(\text{TRPO})_2$  obtained from ground-state DFT calculations. Orbitals of  $\sigma$ -type ( $1b_{3u}$  and  $2b_{3u}$ ) and  $\pi$ -type ( $1b_{1u}$ ,  $1b_{2u}$  and  $2b_{1u}$ ) interactions between O<sub>eq</sub> 2p and U 5f

orbitals and orbitals of  $\pi$ -type ( $1b_{1g}$  and  $1b_{2g}$ ) interactions between O<sub>eq</sub> 2p and U 6d orbitals can be observed in DFT calculations. Orbitals of  $\sigma$ -type bonding interactions between O<sub>eq</sub> 2p and U 6d orbitals in  $a_g$  symmetry are not observable because their energies are too high, resembling the case of  $\text{UO}_2\text{Cl}_4^{2-}$ .<sup>37</sup> The energies of the MOs associated with the bonding interactions between the uranyl ion and TRPO are very similar for the four  $\text{UO}_2\text{Cl}_2(\text{TRPO})_2$  complexes, and this is consistent with the XAS spectra where the substituents have little effect on the pre-edge energies. It is worth mentioning that some orbitals with energies above  $-1.5$  eV contain O 2p components but no U 5f or 6d orbitals. These orbitals also contribute slightly to the pre-edge transitions in the O K-edge XAS, as suggested by TDDFT calculations (*vide infra*).

According to the orbital energies provided by the ground-state DFT calculations in Figure 7, the five pre-edge features (from left to right) around 529.8, 531.4, 533.2, 534.6, and 536.0 eV, obtained by curve-fitting analysis in the O K-edge XAS of the  $\text{UO}_2\text{Cl}_2(\text{TRPO})_2$  complexes in Figure 5, are reasonably assigned to the transitions from O 1s orbitals to the unoccupied MOs of  $1b_{1u} + 1b_{2u} + 1b_{3u}$ ,  $2b_{2u} + 2b_{3u}$ ,  $1b_{1g}$ ,  $2b_{1u}$  and  $1b_{2g} + 1b_{3g}$  symmetries, respectively. The transitions from O 1s orbitals to the unoccupied MOs of  $1b_{1u} + 1b_{2u} + 1b_{3u}$  and  $1b_{1g}$  symmetries are contributed by the oxygen atoms of TRPO. The other three transitions to the orbitals of  $2b_{2u} + 2b_{3u}$ ,  $2b_{1u}$  and  $1b_{2g} + 1b_{3g}$  symmetries are contributed by both the equatorial and axial oxygen atoms. The O<sub>yl</sub> K-edge XAS for the uranyl complexes where no oxygen atoms are present in the equatorial plane have been examined previously.<sup>20,21,67</sup> For example, Denning et al. examined the O<sub>yl</sub> K-edge XAS for  $\text{Cs}_2\text{UO}_2\text{Cl}_4$  and found three pre-edge features at 531.4, 534.1, and 536.5 eV, corresponding to the transitions from O<sub>yl</sub> 1s orbitals to the unoccupied orbitals of U–O<sub>yl</sub> 5f <sub>$\pi$</sub> , U–O<sub>yl</sub> 5f <sub>$\sigma$</sub>  and U–O<sub>yl</sub> 6d <sub>$\pi$</sub>  respectively.<sup>20,21</sup> These values match well with our findings for  $\text{UO}_2\text{Cl}_2(\text{TRPO})_2$  at 531.4 eV, 534.6, and 536.0 eV.

**Hybrid TDDFT Spectral Simulations.** The TDDFT calculations on TRPO and  $\text{UO}_2\text{Cl}_2(\text{TRPO})_2$  are carried out to obtain the simulated spectra for direct comparison with the experiment XAS, and the results are shown in Figure 8. The

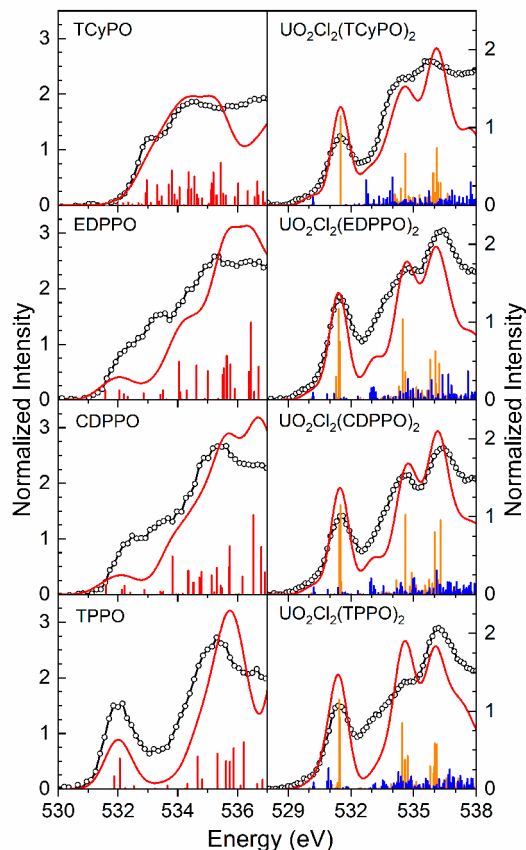


**Figure 8.** Comparison of the simulated spectra obtained by TDDFT calculations (red) with the experimental O K-edge XAS data for TRPO and  $\text{UO}_2\text{Cl}_2(\text{TRPO})_2$  (black). The bars represent the energies and oscillator strengths for the individual transitions. The blue and orange bars represent the transitions from  $\text{O}_{\text{eq}}$  and  $\text{O}_{\text{yl}}$  1s orbitals, respectively, in the TDDFT calculations for  $\text{UO}_2\text{Cl}_2(\text{TRPO})_2$ .

simulated spectra have been shifted by approximately +14.3 eV for TRPO and +12.4 eV for  $\text{UO}_2\text{Cl}_2(\text{TRPO})_2$  to account for the omission of the atomic and extra-atomic relaxation associated with the core excitation, relativistic stabilization, and errors associated with the functional.<sup>68,69</sup>

The simulated spectra of TRPO match well with the experimental data, with a slight discrepancy in relative intensity. The transitions around 532 eV in the simulated spectra for TPPO, CDPPPO, and EDPPPO are not observed for TCyPO, consistent with the experimental spectra. The TDDFT simulations confirm that the pre-edge regions from 533 to 536 eV in the O K-edge XAS spectra for TRPO are attributed to the electronic transitions from O 1s orbitals to the unoccupied MOs formed by the mixing of R  $\sigma$ -orbitals with  $\text{P}=\text{O}$  ( $\sigma + \pi$ )-orbitals.

For the spectra of  $\text{UO}_2\text{Cl}_2(\text{TRPO})_2$ , the electronic transitions from  $\text{O}_{\text{eq}}$  and  $\text{O}_{\text{yl}}$  1s orbitals to the unoccupied MOs were calculated separately, and the transitions are depicted by blue and orange bars, respectively, in Figure 8. One can see that five transition features in TDDFT simulated spectra are resolved, matching well with the experimental data.

Although there is no way to experimentally discriminate the contributions from  $\text{O}_{\text{eq}}$  and  $\text{O}_{\text{yl}}$  atoms to the XAS spectra of  $\text{UO}_2\text{Cl}_2(\text{TRPO})_2$ , TDDFT calculations confirm the assignments of transitions in DFT calculations that the first feature at 529.8 eV in each spectrum is entirely attributed to the transitions from  $\text{O}_{\text{eq}}$  1s orbitals to the unoccupied MOs of  $1b_{1u} + 1b_{2u} + 1b_{3u}$  symmetries, which are associated with the covalent mixing between  $\text{O}_{\text{eq}}$  2p orbitals and U 5f orbitals. The transitions from  $\text{O}_{\text{eq}}$  and  $\text{O}_{\text{yl}}$  1s orbitals to unoccupied MOs both contribute to the pre-edge features at 531.4, 534.6, and 536.0 eV obtained by curve fits in Figure 5, with  $\text{O}_{\text{yl}}$  contributing much more than  $\text{O}_{\text{eq}}$ . The pre-edge feature around 533.2 eV is contributed by the transition from  $\text{O}_{\text{eq}}$  1s orbitals to the orbital of  $1b_{1g}$  symmetry, and there are no transitions from  $\text{O}_{\text{yl}}$  1s orbitals to the unoccupied orbitals. As mentioned above, some orbitals containing O 2p components that do not mix with U 5f or 6d orbitals can contribute slightly to the pre-edge transitions from O 1s orbitals to the orbitals of  $1b_{1g}$  symmetry as well as to those of  $2b_{2u} + 2b_{3u}$ ,  $2b_{1u}$ , and  $1b_{2g} + 1b_{3g}$  symmetries. In such a context, only the transitions from O 1s orbitals to the orbitals of  $1b_{1u} + 1b_{2u} + 1b_{3u}$  symmetries exclusively reflect the U– $\text{O}_{\text{eq}}$  covalent bonding interactions.

**Evaluation of the Bonding Covalency between the Uranyl Ion and TRPO.** The intensity of the pre-edge feature observed in ligand K-edge XAS spectra correlates to the degree of ligand  $np$  orbital mixing in metal-derived MOs according to the relationship<sup>29,70</sup>

$$I = \frac{1}{N} h \alpha^2 I_0 \quad (1)$$

where  $I$  is the integrated pre-edge area for the normalized spectrum,  $N$  is the number of absorbing ligand atoms,  $h$  is the number of electron holes,  $\alpha^2$  is the p character per electron-hole in the acceptor molecular orbital, and  $I_0$  is the intrinsic transition dipole integral for ligand  $1s \rightarrow np$  excitations that is dependent on the property of the sample, sample preparation, detection method, and beamline end-station and upstream optics. To obtain  $\alpha^2$  from the pre-edge intensity requires the value of the intrinsic transition dipole integral  $I_0$ . In the quantitative study of lanthanide-oxygen orbital mixing in  $\text{CeO}_2$ ,  $\text{PrO}_2$ , and  $\text{TbO}_2$ , Minasian et al. compared the pre-edge intensities associated with Ln 4f orbitals in the O K-edge XAS spectra to the relative intensities of the two peaks in the Ln  $L_{3-}$  edge XAS and estimated a value of 9.86 for the intrinsic intensity of O  $1s \rightarrow 2p$  transition.<sup>46</sup> This value is comparable to 10.3 for the photoabsorption cross-section of atomic oxygen reported by McLaughlin et al.<sup>71</sup> As mentioned above, many factors affect the intrinsic intensity of  $I_0$ , such as the sample properties and detection method. In this work, the method to collect the XAS spectra is TFY, in which the intrinsic intensity is proportional to the X-ray absorption cross section. Saturation and self absorption effects must be considered because they can cause fluorescence yield variations, resulting in the variation of the pre-edge transition intensities.<sup>72,73</sup> Besides, the effective charge dependence of the transition dipole moment integral should be taken into account, as reported by Neese et al.<sup>74</sup> In this context, it is not appropriate to directly convert the experimental pre-edge intensity of the O K-edge XAS in Figure 5 to percent O 2p character using the value of the intrinsic intensity obtained from lanthanide dioxides or atomic oxygen. In this work, therefore, we use the data from Mulliken population analysis that are intimately

associated with the experimental XAS data to evaluate the bonding covalency between the uranyl ion and TRPO ligands. Table 2 summarizes the DFT calculated percent  $O_{eq}$  and  $O_{yl}$  2p character for the MOs showing in Figure 7 that are relevant

**Table 2. Mulliken Population Analysis for the  $UO_2Cl_2(TRPO)_2$  Complexes**

MO <sup>a</sup>	energy (eV)	Mulliken population (DFT, %)		
		O <sub>eq</sub> 2p	O <sub>yl</sub> 2p	Cl 3p
UO <sub>2</sub> Cl <sub>2</sub> (TPPO) <sub>2</sub>				
1b <sub>1u</sub>	−2.19	0.39		2.51
1b <sub>2u</sub>	−2.17	1.00		4.37
1b <sub>3u</sub>	−2.15	0.35		3.67
2b <sub>2u</sub>	−0.50		21.19	2.43
2b <sub>3u</sub>	−0.49	0.16	18.97	
1b <sub>1g</sub>	0.79	1.00		5.60
2b <sub>1u</sub>	2.88	0.37	37.31	0.26
1b <sub>2g</sub>	3.93	0.26	8.93	
1b <sub>3g</sub>	4.00		9.24	2.64
UO <sub>2</sub> Cl <sub>2</sub> (CDPPO) <sub>2</sub>				
1b <sub>1u</sub>	−2.31	0.64		2.35
1b <sub>2u</sub>	−2.29	1.10		4.63
1b <sub>3u</sub>	−2.26	0.20		3.68
2b <sub>2u</sub>	−0.64		20.85	2.50
2b <sub>3u</sub>	−0.69	0.01	18.99	
1b <sub>1g</sub>	0.70	1.15		5.02
2b <sub>1u</sub>	2.64	0.37	15.24	0.03
1b <sub>2g</sub>	3.87	0.23	7.65	
1b <sub>3g</sub>	3.90		7.83	0.66
UO <sub>2</sub> Cl <sub>2</sub> (EDPPO) <sub>2</sub>				
1b <sub>1u</sub>	−2.30	0.41		2.61
1b <sub>2u</sub>	−2.26	1.13		4.62
1b <sub>3u</sub>	−2.23	0.52		3.74
2b <sub>2u</sub>	−0.64		20.92	2.54
2b <sub>3u</sub>	−0.63	0.19	18.80	
1b <sub>1g</sub>	0.72	1.31		5.39
2b <sub>1u</sub>	2.75	0.39	19.52	0.29
1b <sub>2g</sub>	3.82	0.26	10.01	
1b <sub>3g</sub>	3.98		9.03	1.32
UO <sub>2</sub> Cl <sub>2</sub> (TCyPO) <sub>2</sub>				
1b <sub>1u</sub>	−2.14	0.65		2.32
1b <sub>2u</sub>	−2.11	1.28		4.58
1b <sub>3u</sub>	−2.08	0.42		3.66
2b <sub>2u</sub>	−0.55		20.69	2.56
2b <sub>3u</sub>	−0.51	0.01	18.92	
1b <sub>1g</sub>	0.80	0.50		4.41
2b <sub>1u</sub>	2.68	0.16	10.07	0.06
1b <sub>2g</sub>	3.93	0.68	5.51	
1b <sub>3g</sub>	4.03		6.31	2.75

<sup>a</sup>Orbitals at high energy levels, e.g.,  $2b_{1u}$ ,  $1b_{2g}$ , and  $1b_{3g}$ , split into two or more orbitals, among which the highest orbital composition is presented in the table.

to the pre-edge transitions in the O K-edge XAS of the  $UO_2Cl_2(TRPO)_2$  complexes. Taking  $UO_2Cl_2(TPPO)_2$  as an example, the amount of  $O_{eq}$  2p character in the  $\pi$ -bonding with U 5f orbitals of  $1b_{1u}$ ,  $1b_{2u}$ , and  $2b_{1u}$  symmetries are 0.39, 1.00, and 0.37, respectively, and that in the  $\sigma$ -bonding with U 5f orbitals of  $1b_{3u}$  and  $2b_{3u}$  symmetries are 0.35 and 0.16, respectively. The amount of  $O_{eq}$  2p character in the  $\pi$ -bonding with U 6d orbitals of  $1b_{1g}$  and  $1b_{2g}$  symmetries are 1.00 and 0.26, respectively. All the amounts of  $O_{eq}$  2p character are very

small and much lower than that of  $O_{yl}$  2p character. For example, the amount of  $O_{yl}$  2p character in  $\pi$ -bonding with U 5f orbitals of  $2b_{2u}$  and  $2b_{3u}$  symmetries are 21.19 and 18.97, respectively. Upon the variation of the TRPO ligands in the  $UO_2Cl_2(TRPO)_2$  complexes, the amounts of  $O_{eq}$  2p character are very similar, indicating the insignificant effect of the substituents in TRPO on the bonding interaction with the uranyl ion.

As mentioned above, only the pre-edge feature around 529.8 eV in each spectrum is exclusively attributed to the transitions from  $O_{eq}$  1s orbitals to the unoccupied MOs of  $1b_{1u} + 1b_{2u} + 1b_{3u}$  symmetries. The total amount of  $O_{eq}$  2p character of the orbitals of  $1b_{1u} + 1b_{2u} + 1b_{3u}$  symmetries in Mulliken population are 1.74, 1.94, 2.06, and 2.37% in  $UO_2Cl_2(TPPO)_2$ ,  $UO_2Cl_2(CDPPO)_2$ ,  $UO_2Cl_2(EDPPO)_2$ , and  $UO_2Cl_2(TCyPO)_2$ , respectively. These small values are consistent with the small intensity of the first pre-edge feature in the O K-edge XAS spectra for the  $UO_2Cl_2(TRPO)_2$  complexes. In contrast, the total amount of  $O_{yl}$  2p character in the orbitals of  $2b_{2u} + 2b_{3u}$  symmetries in Mulliken population are remarkably large, corresponding to the high intensity of the pre-edge features around 531.4 eV in the O K-edge XAS of the  $UO_2Cl_2(TRPO)_2$  complexes. In general, both the experimental O K-edge XAS results and DFT calculations clearly indicate a very small amount of covalent bonding between the uranyl ions and TRPO ligands in the  $UO_2Cl_2(TRPO)_2$  complexes.

Although there have been many studies on the interactions between the uranyl ion and ligands on its equatorial plane, few have evaluated the bonding covalency. Spencer et al. examined the Cl K-edge XAS for  $[Ph_4P]_2[UO_2Cl_4]$  and found that the total amount of percent Cl 3p character observed with the U 5f orbitals was roughly 7.6% per U–Cl bond.<sup>37</sup> According to the intensities of the pre-edge features obtained by curve-fitting analysis on the Cl K-edge XAS for the  $UO_2Cl_2(TRPO)_2$  complexes (Figure S6 and Tables S7 and S8), the amount of percent Cl 3p character with the U 5f orbitals is from 6.53 to 8.02 per U–Cl bond in the  $UO_2Cl_2(TRPO)_2$  complexes. DFT calculations (Table 2) reveal that the total amount of Cl 3p character in the orbitals of  $1b_{1u} + 1b_{2u} + 1b_{3u} + 2b_{2u}$  symmetries are 12.98, 13.16, 13.51, and 13.12, corresponding to 6.49, 6.58, 6.76, and 6.56 per U–Cl bond in  $UO_2Cl_2(TPPO)_2$ ,  $UO_2Cl_2(CDPPO)_2$ ,  $UO_2Cl_2(EDPPO)_2$ , and  $UO_2Cl_2(TCyPO)_2$ , respectively. The XAS experiments and DFT calculations agree very well with each other. The Mulliken population analysis suggests that the U 5f orbitals participate more in mixing with Cl 3p orbitals than in mixing with  $O_{eq}$  2p orbitals in the  $UO_2Cl_2(TRPO)_2$  complexes. Furthermore, both the experimental and theoretical results quantitatively confirm the conclusion aforementioned that the interactions of Cl 3p orbitals with the U 5f and 6d orbitals are not significantly perturbed when varying the other equatorial ligands in the uranyl complexes.

## CONCLUSION AND OUTLOOK

We have detected for the first time the covalency of the U(VI)–TRPO system that is actually used in separation processes using the technique of oxygen K-edge X-ray absorption spectroscopy (XAS) in combination with density functional theory (DFT) calculations. The primary purpose of this work is to investigate the contributions of U 6d and especially 5f orbitals to the bonding covalency between the uranyl ion and TRPO on its equatorial plane in order to

elucidate the extraordinary extractability and selectivity of the monodentate organophosphorus extractants to the uranyl ion. Using the O K-edge XAS technique and DFT calculations, we have detected the electronic structure of both the free ligands TRPO and the complexes  $\text{UO}_2\text{Cl}_2(\text{TRPO})_2$ . Although the TRPO ligands display substantially different pre-edge features depending on whether their substituents can provide  $\pi$ -orbitals to mix with the  $\text{O}=\text{P}$  orbitals, all the TRPO investigated can engage in  $\sigma$ - and  $\pi$ -type interactions with U 5f and 6d orbitals in the  $\text{UO}_2\text{Cl}_2(\text{TRPO})_2$  complexes. All the  $\text{UO}_2\text{Cl}_2(\text{TRPO})_2$  complexes show similar pre-edge features in O K-edge XAS, indicating that substituents on TRPO have little effect on the covalent bonding between TRPO and  $\text{UO}_2^{2+}$ . The first pre-edge feature in the O K-edge XAS of  $\text{UO}_2\text{Cl}_2(\text{TRPO})_2$  is identified as the transitions to the U 5f orbitals of  $1b_{1u} + 1b_{2u} + 1b_{3u}$  symmetries, which are exclusively contributed by the  $\sigma$ - and  $\pi$ -type mixing between U 5f and  $\text{O}_{\text{eq}}$  2p orbitals. Curve-fitting analysis indicates small intensities of 0.12–0.14 for this pre-edge feature of the  $\text{UO}_2\text{Cl}_2(\text{TRPO})_2$  complexes, which are consistent with the small amount of  $\text{O}_{\text{eq}}$  2p character (1.74–2.37%) as obtained by Mulliken population analysis. Other pre-edge features in the O K-edge XAS of  $\text{UO}_2\text{Cl}_2(\text{TRPO})_2$  are dominantly contributed by the  $\text{U}-\text{O}_{\text{yl}}$  orbital mixing, and the contributions of the  $\text{U}-\text{O}_{\text{eq}}$  orbital mixing cannot be extracted from the experimental spectra. Nonetheless, DFT calculations reveal that both U 5f and 6d orbitals can participate in U–TRPO  $\sigma$ - and  $\pi$ -type covalent bonding interactions.

To thoroughly reveal the role of covalency in extraction separation, additional work is warranted in the future, as there are many factors that can affect the extraction efficiency, such as the geometries of the extracted species and the aggregation behavior in the organic phase. Nevertheless, we believe that the covalent bonding interactions between TRPO and  $\text{UO}_2^{2+}$ , especially the contributions from U 5f orbitals, play the central role in achieving the remarkable extractability and selectivity of TRPO for the uranyl ion. Cross et al. reported that the amount of Cl 3p character mixing with Am 5f orbitals is 0.54(5)% per Am–Cl bond for  $\text{AmCl}_6^{3-}$ . In contrast, for  $\text{EuCl}_6^{3-}$  the amount of Cl 3p orbital mixing in the Eu–Cl bond is too small to quantify and significantly less than the 0.54(5)% value for  $\text{AmCl}_6^{3-}$ . The subtle differences between Am 5f orbitals in Am–Cl orbital mixing and Eu 4f orbitals in Eu–Cl orbital mixing are considered to have the potential to achieve the appreciable Am/Eu separations,<sup>38</sup> because only ~0.4 kcal/mol/bond is needed to achieve appreciable Am/Eu separations.<sup>75</sup> In the present work, the total amount of mixing between U 5f and  $\text{O}_{\text{eq}}$  2p orbitals is 0.87–1.18% per U– $\text{O}_{\text{eq}}$  bond as obtained by Mulliken population analysis. This value is relatively small, but it is supposed to be sufficiently significant for achieving a high distribution ratio in an extraction, according to the work by Cross and co-workers.<sup>38</sup> In contrast, it is not necessarily the case that more covalency would induce stronger interactions between metal ions and ligands. Covalent interactions between the ligands and metal ions are usually accompanied by ligand-to-metal charge transfer interactions, which would act to weaken the stabilization of the metal–ligand complexes due to the reduced ionic attraction by decreasing the charge differential.<sup>76</sup> Therefore, too much covalency between the ligands and metal ions can be counterproductive to extraction and separation. This is reminiscent of the multidentate ligands with both hard and soft donor atoms that possess high extractability and selectivity

toward actinides. The soft donor atoms play the role to covalently interact with the metal ions to enhance the selectivity in extraction, while the hard donor atoms retain the affinity and thus the remarkable extractability toward the metal ions.<sup>77–81</sup> Accordingly, the TRPO ligands can serve the combined soft–hard strategy in the extraction of uranyl ions, in which a small amount of covalency based on the strong affinity achieve the remarkable selectivity and extractability of TRPO toward the uranyl ions.

## EXPERIMENTAL SECTION

**Sample Preparation.** *Caution!* Standard precautions for handling radioactive materials should be implemented due to the slightly radioactive uranium used in this work.

Single crystals of TRPO suitable for X-ray diffraction characterization were obtained by recrystallization from dichloromethane/*n*-heptane in a glovebox, according to the procedure reported in the literature.<sup>56</sup> Single crystals of the uranyl complexes  $\text{UO}_2\text{Cl}_2(\text{TRPO})_2$  were prepared using the reported procedures with slight modifications.<sup>13</sup> Detailed procedures for the synthesis of  $\text{UO}_2\text{Cl}_2(\text{TRPO})_2$  are illustrated in the Supporting Information.  $[\text{PPh}_4]_2[\text{UO}_2\text{Cl}_4]$  was synthesized and crystallized from the reaction of hydrated uranyl nitrate with tetraphenylphosphonium chloride in acetonitrile followed by slow evaporation in atmosphere condition based on the reports in the literature with some modification.<sup>82,83</sup>

**X-ray Crystallography.** The single-crystal X-ray diffraction data were collected on a Super Nova, Dual, Cu at zero, AtlasS2 (Rigaku) using Cu K $\alpha$  ( $\lambda = 1.54184$  Å) or Mo K $\alpha$  ( $\lambda = 0.71073$  Å) radiation. All crystals were measured at low temperature (104–173 K). Data collection and reduction were carried out in CrysAlisPro 1.171.39.46 (Rigaku Oxford Diffraction, 2018). The structure solution and refinement were carried out with SHLEX-97 and Olex2 1.2 program.<sup>84,85</sup> The absorption data were corrected using the multiscan method. The structure was solved by direct methods or Intrinsic Phasing method and was refined against  $F^2$  by full-matrix least-squares techniques. All non-hydrogen atoms were refined with anisotropic displacement parameters. The hydrogen atoms were added according to the ideal geometry and were not refined for good refinement convergence. Data collection and refinement details are available in Tables S1 and S2. The crystallographic information files (CIFs) mentioned this manuscript are available through the Cambridge Crystal Data Centre (CCDC 2043630–2043637).

**XAS Measurements and Data Analysis.** The O K-edge XAS data were recorded at beamline 02B02 of Shanghai Synchrotron Radiation Facility (SSRF) running in electron storage ring mode at 3.5 GeV and with current at 240 mA.<sup>86</sup> The energy range of the beamline 02B02 is from 40 to 2000 eV. The measured photon flux is around  $10^{11}$  photons/s with  $E/\Delta E = 3700$  at 244 eV. The beam spot size at a sample is measured to be about  $150 \mu\text{m} \times 50 \mu\text{m}$ . Grating was optimized with line densities of 400 lines  $\text{mm}^{-1}$  covering the energy ranges 40–600 eV to obtain high-energy resolution. The XAS data were collected by total fluorescence yield (TFY) mode in an ultrahigh vacuum chamber about  $5 \times 10^{-9}$  Torr. The energy steps of 1, 0.15, 0.3, 1, and 2 eV were used between 500 and 530, 530–545, 545–560, 560–580, and 580–600 eV, respectively, to collect the O K-edge XAS data. The P and Cl K-edge XAS data were recorded at beamline 4B7A of Beijing Synchrotron Radiation Facility (BSRF) over an energy range from 1750 to 6000 eV in partial fluorescence yield (PFY) mode using a 13-element Si (Li) array detector.<sup>87</sup> The energy of the electron beam is 2.5 GeV in the storage ring, where the maximum beam current is 250 mA. The beam spot size at a sample is about  $1.5 \text{ mm} \times 0.4 \text{ mm}$ , and the measured flux is over  $3 \times 10^{10}$  photons/s/250 mA.

Single-crystal samples were ground into a fine powder and dispersed on carbon tape for P and Cl K-edge XAS measurements and indium films for O K-edge XAS measurements. The energy scales in the O, P, and Cl K-edge XAS were calibrated using  $\text{SrTiO}_3$ ,  $\text{Na}_4\text{P}_2\text{O}_7$ , and  $\text{D}_{2d}\text{-Cs}_2\text{CuCl}_4$  standard, respectively, which were

656 repeatedly analyzed between sample scans. All the spectra were  
657 collected in duplicate at least twice. Spectra showed no signs of  
658 radiation damage and were reproduced over multiple regions of the  
659 sample.

660 The background subtraction and normalization of O, P, and Cl K-  
661 edge XAS data were manipulated using the Athena interface in the  
662 Demeter software program.<sup>88</sup> In a typical example, a line was fit to the  
663 pre-edge region and then subtracted from the experimental data to  
664 eliminate the background of the spectrum. The data were normalized  
665 to a unit step height by fitting a second-order polynomial to the  
666 postedge region of the spectrum. Curve-fitting of the O K-edge XAS  
667 was carried out using the program IGOR pro 8.04 and a modified  
668 version of EDG\_FIT.<sup>89</sup> Second derivative spectra were used as guides  
669 to determine the number and position of peaks (Figures S1 and S3).  
670 Pre-edge and rising edge features were modeled by Gaussian line  
671 shapes and an error function, respectively (Figures S2 and S4). Fits  
672 were carried out over several energy ranges. The quality of each curve  
673 fit was determined by evaluating changes in the  $\chi^2$  and by inspecting  
674 the residual intensity, which is obtained by subtracting the fit from the  
675 experiment data and should resemble a horizontal line at zero. The  
676 area under the pre-edge peaks (defined as the intensity) was used as  
677 the transition intensity.

678 **DFT and TDDFT Calculation.** All DFT computations were  
679 carried out with the Amsterdam Density Functional (ADF 2019)  
680 program,<sup>90,91</sup> using the B3LYP hybrid functional.<sup>92,93</sup> The all-electron  
681 Slater type orbital (STO) basis sets of triple- $\zeta$  augmented by two sets  
682 of polarization functions (TZ2P) were employed to describe all  
683 atoms. Zero-order regular approximation (ZORA) was used to  
684 consider the scalar relativistic (SR) effects.<sup>94</sup> The geometries were  
685 optimized for TRPO and  $\text{UO}_2\text{Cl}_2(\text{TRPO})_2$ , and the selected average  
686 bond lengths and bond angles were comparable to the values in the  
687 experimental crystals (Tables S3 and S4). To obtain the values of  
688 Mulliken populations larger than 0.01%, the keyword "ORBPOP" was  
689 used in single-point calculations.

690 The O K-edge XAS spectra for all complexes were simulated using  
691 of simplified TDDFT (sTDDFT) method.<sup>95,96</sup> For the TDDFT  
692 calculations at the ground-state optimized geometry, only excitations  
693 from O 1s core levels to virtual orbitals were analyzed by restricting  
694 the energy range of core level and virtual orbitals involved in  
695 excitation. The calculated oscillator strengths were evenly broadened  
696 with a Gaussian function of full-width at half maximum of 1 eV to  
697 generate the simulated absorption spectra. An energy shift was applied  
698 by aligning the experimental and calculated pre-edge peaks to account  
699 for the omission of the atomic and extra-atomic relaxation associated  
700 with the core excitation, relativistic stabilization, and errors associated  
701 with the functional, according to the literature.<sup>68,69</sup>

## 702 ■ ASSOCIATED CONTENT

### 703 ■ Supporting Information

704 The Supporting Information is available free of charge at  
705 <https://pubs.acs.org/doi/10.1021/acs.inorgchem.1c02236>.

706 Experiments and results for the solvent extraction of the  
707 uranyl ion by the ligands used in the present work,  
708 detailed procedure for the crystallization of the  
709  $\text{UO}_2\text{Cl}_2(\text{TRPO})_2$  complexes, crystallographic data,  
710 bond lengths and bond angles for the TRPO and  
711  $\text{UO}_2\text{Cl}_2(\text{TRPO})_2$  complexes, complete curve-fitting of  
712 the XAS spectra, and the analysis of the Cl K-edge XAS  
713 for the  $\text{UO}_2\text{Cl}_2(\text{TRPO})_2$  complexes (PDF)

### 714 Accession Codes

715 CCDC 2043630–2043637 contain the supplementary crys-  
716 tallographic data for this paper. These data can be obtained  
717 free of charge via [www.ccdc.cam.ac.uk/data\\_request/cif](http://www.ccdc.cam.ac.uk/data_request/cif), or by  
718 emailing [data\\_request@ccdc.cam.ac.uk](mailto:data_request@ccdc.cam.ac.uk), or by contacting The  
719 Cambridge Crystallographic Data Centre, 12 Union Road,  
720 Cambridge CB2 1EZ, UK; fax: +44 1223 336033.

## 721 ■ AUTHOR INFORMATION

### 722 Corresponding Author

723 Taoxiang Sun – Institute of Nuclear and New Energy  
724 Technology, Tsinghua University, Beijing 100084, China;  
725 [orcid.org/0000-0003-4690-3566](https://orcid.org/0000-0003-4690-3566); Email: [sunstx@](mailto:sunstx@tsinghua.edu.cn)  
726 [tsinghua.edu.cn](mailto:sunstx@tsinghua.edu.cn)

### 727 Authors

728 Yusheng Zhang – Institute of Nuclear and New Energy  
729 Technology, Tsinghua University, Beijing 100084, China  
730 Wuhua Duan – Institute of Nuclear and New Energy  
731 Technology, Tsinghua University, Beijing 100084, China  
732 Yuning Yang – Institute of Nuclear and New Energy  
733 Technology, Tsinghua University, Beijing 100084, China  
734 Tian Jian – Chemical Sciences Division, Lawrence Berkeley  
735 National Laboratory, Berkeley, California 94720, United  
736 States; [orcid.org/0000-0002-2448-4666](https://orcid.org/0000-0002-2448-4666)  
737 Yusen Qiao – Chemical Sciences Division, Lawrence Berkeley  
738 National Laboratory, Berkeley, California 94720, United  
739 States; [orcid.org/0000-0001-7654-8636](https://orcid.org/0000-0001-7654-8636)  
740 Guoxi Ren – Shanghai Institute of Microsystem and  
741 Information Technology, Chinese Academy of Sciences,  
742 Shanghai 200050, China  
743 Nian Zhang – Shanghai Institute of Microsystem and  
744 Information Technology, Chinese Academy of Sciences,  
745 Shanghai 200050, China; [orcid.org/0000-0002-9124-](https://orcid.org/0000-0002-9124-6553)  
746 [6553](https://orcid.org/0000-0002-9124-6553)  
747 Lei Zheng – Institute of High Energy Physics, Chinese  
748 Academy of Sciences, Beijing 100049, China  
749 Wensheng Yan – University of Science and Technology of  
750 China, National Synchrotron Radiation Laboratory, Hefei  
751 230029, China; [orcid.org/0000-0001-6297-4589](https://orcid.org/0000-0001-6297-4589)  
752 Jianchen Wang – Institute of Nuclear and New Energy  
753 Technology, Tsinghua University, Beijing 100084, China  
754 Jing Chen – Institute of Nuclear and New Energy Technology,  
755 Tsinghua University, Beijing 100084, China  
756 Stefan G. Minasian – Chemical Sciences Division, Lawrence  
757 Berkeley National Laboratory, Berkeley, California 94720,  
758 United States; [orcid.org/0000-0003-1346-7497](https://orcid.org/0000-0003-1346-7497)

759 Complete contact information is available at:

760 <https://pubs.acs.org/doi/10.1021/acs.inorgchem.1c02236>

### 761 Notes

762 The authors declare no competing financial interest.

## 763 ■ ACKNOWLEDGMENTS

764 This study is supported by the National Natural Science  
765 Foundation of China (21976103 and U1830202). S.G.M. was  
766 supported by the Director, Office of Science, Office of Basic  
767 Energy Sciences, Division of Chemical Sciences, Geosciences,  
768 and Biosciences (CSGB), Heavy Element Chemistry program  
769 of the U.S. Department of Energy (DOE) under contract no.  
770 DE-AC02-05CH11231 at LBNL. We are grateful to Ming Li  
771 (Tsinghua University) for his help with the single-crystal  
772 structures and Zhixian Wang (Peking University) for her help  
773 with the element analysis. The XAS data in this work were  
774 carried out with the support of 02B02 beamline of Shanghai  
775 Synchrotron Radiation Facility (SSRF), 4B7A beamline at  
776 Beijing Synchrotron Radiation Facility, and BL12B beamline of  
777 National Synchrotron Radiation Laboratory (NSRL) of China.

## 778 ■ REFERENCES

- (1) Mathur, J. N.; Murali, M. S.; Nash, K. L. Actinide partitioning - A review. *Solvent Extr. Ion Exch.* **2001**, *19* (3), 357–390.
- (2) Beltrami, D.; Cote, G.; Mokhtari, H.; Courtaud, B.; Moyer, B. A.; Chagnes, A. Recovery of uranium from wet phosphoric acid by solvent extraction processes. *Chem. Rev.* **2014**, *114* (24), 12002–12023.
- (3) Abney, C. W.; Mayes, R. T.; Saito, T.; Dai, S. Materials for the recovery of uranium from seawater. *Chem. Rev.* **2017**, *117* (23), 13935–14013.
- (4) Keener, M.; Hunt, C.; Carroll, T. G.; Kampel, V.; Dobrovetsky, R.; Hayton, T. W.; Menard, G. Redox-switchable carboranes for uranium capture and release. *Nature* **2020**, *577* (7792), 652–655.
- (5) Leoncini, A.; Huskens, J.; Verboom, W. Ligands for f element extraction used in the nuclear fuel cycle. *Chem. Soc. Rev.* **2017**, *46*, 7229–7273.
- (6) Chen, J.; He, X. H.; Wang, J. C. Nuclear fuel cycle-oriented actinides separation in China. *Radiochim. Acta* **2014**, *102* (1–2), 41–51.
- (7) Bombieri, G.; Forsellini, E.; Day, J. P.; Azeez, W. I. Crystal and molecular-structure of "dichlorodioxobis(triphenylphosphine oxide)-uranium(VI). *J. Chem. Soc., Dalton Trans.* **1978**, *6*, 677–680.
- (8) Akona, S. B.; Fawcett, J.; Holloway, J. H.; Russell, D. R.; Leban, I. Structures of cis and trans-dichlorodioxobis(triphenylphosphine oxide)-uranium(VI). *Acta Crystallogr., Sect. C: Cryst. Struct. Commun.* **1991**, *47*, 45–48.
- (9) Arnaiz, F. J.; Miranda, M. J. Microscale synthesis of  $\text{UO}_2\text{Cl}_2(\text{OPPh}_3)_2$ . *J. Chem. Educ.* **1998**, *75* (11), 1457–1458.
- (10) Crawford, M. J.; Ellern, A.; Karaghiosoff, K.; Mayer, P.; Noth, H.; Suter, M. Synthesis and characterization of heavier dioxouranium(VI) dihalides. *Inorg. Chem.* **2004**, *43* (22), 7120–7126.
- (11) Haller, L. J. L.; Kaltsayannis, N.; Sarsfield, M. J.; May, I.; Cornet, S. M.; Redmond, M. P.; Helliwell, M. A structural and theoretical investigation of equatorial cis and trans uranyl phosphinimine and uranyl phosphine oxide complexes  $\text{UO}_2\text{Cl}_2(\text{Cy}_3\text{PNH})_2$  and  $\text{UO}_2\text{Cl}_2(\text{Cy}_3\text{PO})_2$ . *Inorg. Chem.* **2007**, *46* (12), 4868–4875.
- (12) Redmond, M. P.; Cornet, S. M.; Woodall, S. D.; Whittaker, D.; Collison, D.; Helliwell, M.; Natrajan, L. S. Probing the local coordination environment and nuclearity of uranyl(VI) complexes in non-aqueous media by emission spectroscopy. *Dalton Trans.* **2011**, *40* (15), 3914–3926.
- (13) Hashem, E.; McCabe, T.; Schulzke, C.; Baker, R. J. Synthesis, structure and photophysical properties of  $\text{UO}_2 \times 2(\text{O}=\text{PPh}_3)_2$  (X = Cl, Br, I). *Dalton Trans.* **2014**, *43* (3), 1125–1131.
- (14) Hutschka, F.; Dedieu, A.; Troxler, L.; Wipff, G. Theoretical studies on the  $\text{UO}_2^{2+}$  and  $\text{Sr}^{2+}$  complexation by phosphoryl-containing  $\text{O}=\text{PR}_3$  ligands: QM ab initio calculations in the gas phase and MD FEP calculations in aqueous solution. *J. Phys. Chem. A* **1998**, *102* (21), 3773–3781.
- (15) Arnaiz, F. J.; Miranda, M. J.; Aguado, R.; Mahia, J.; Maestro, M. A. Synthesis and molecular structure of the all-trans- and the trans-cis-  $\text{UO}_2\text{Br}_2(\text{OAsPh}_3)_2$  isomers. *Polyhedron* **2001**, *20* (28), 3295–3299.
- (16) Wang, C. Z.; Lan, J. H.; Zhao, Y. L.; Chai, Z. F.; Wei, Y. Z.; Shi, W. Q. Density functional theory studies of  $\text{UO}_2^{2+}$  and  $\text{NpO}_2^{2+}$  complexes with carbamoylmethylphosphine oxide ligands. *Inorg. Chem.* **2013**, *52* (1), 196–203.
- (17) Vats, B. G.; Kannan, S.; Parvathi, K.; Maity, D. K.; Drew, M. G. B. Steric effects in complexes of diphenyl(2-pyridyl)phosphine oxide with the uranyl ion. Synthetic, structural and theoretical studies. *Polyhedron* **2015**, *89*, 116–121.
- (18) Raychaudhuri, D.; Gopakumar, G.; Nagarajan, S.; Brahmmananda Rao, C. V. S. On the nature of the carbonyl versus phosphoryl binding in uranyl nitrate complexes. *J. Phys. Chem. A* **2020**, *124* (38), 7805–7815.
- (19) Denning, R. G. Electronic-structure and bonding in actinyl ions. *Struct. Bonding (Berlin)* **1992**, *79*, 215–276.
- (20) Denning, R. G.; Green, J. C.; Hutchings, T. E.; Dallera, C.; Tagliaferri, A.; Giarda, K.; Brookes, N. B.; Braicovich, L. Covalency in the uranyl ion: A polarized X-ray spectroscopic study. *J. Chem. Phys.* **2002**, *117* (17), 8008–8020.
- (21) Denning, R. G. Electronic structure and bonding in actinyl ions and their analogs. *J. Phys. Chem. A* **2007**, *111* (20), 4125–4143.
- (22) Cowie, B. E.; Purkis, J. M.; Austin, J.; Love, J. B.; Arnold, P. L. Thermal and photochemical reduction and functionalization chemistry of the uranyl dication,  $[\text{U}(\text{VI})\text{O}_2]^{2+}$ . *Chem. Rev.* **2019**, *119* (18), 10595–10637.
- (23) Dau, P. D.; Su, J.; Liu, H.-T.; Huang, D.-L.; Li, J.; Wang, L.-S. Photoelectron spectroscopy and the electronic structure of the uranyl tetrachloride dianion:  $\text{UO}_2\text{Cl}_4^{2-}$ . *J. Chem. Phys.* **2012**, *137* (6), No. 064315.
- (24) Su, J.; Dau, P. D.; Qiu, Y. H.; Liu, H. T.; Xu, C. F.; Huang, D. L.; Wang, L. S.; Li, J. Probing the electronic structure and chemical bonding in tricoordinate uranyl complexes  $\text{UO}_2 \times 3-$  (X = F, Cl, Br, I): Competition between Coulomb repulsion and U-X bonding. *Inorg. Chem.* **2013**, *52* (11), 6617–6626.
- (25) Liu, J. B.; Chen, G. P.; Huang, W.; Clark, D. L.; Schwarz, W. H. E.; Li, J. Bonding trends across the series of tricarbonate-actinyl anions  $(\text{AnO}_2)(\text{CO}_3)_3(4-)$  (An = U-Cm): the plutonium turn. *Dalton Trans.* **2017**, *46* (8), 2542–2550.
- (26) Odoh, S. O.; Schreckenbach, G. DFT study of uranyl peroxo complexes with  $\text{H}_2\text{O}$ , F-, OH-,  $\text{CO}_3^{2-}$ , and  $\text{NO}_3^-$ . *Inorg. Chem.* **2013**, *52* (9), 5590–5602.
- (27) Choppin, G. R. Covalency in f element bonds. *J. Alloys Compd.* **2002**, *344* (1–2), 55–59.
- (28) Neidig, M. L.; Clark, D. L.; Martin, R. L. Covalency in f element complexes. *Coord. Chem. Rev.* **2013**, *257* (2), 394–406.
- (29) Solomon, E. I.; Hedman, B.; Hodgson, K. O.; Dey, A.; Szilagyi, R. K. Ligand K-edge X-ray absorption spectroscopy: covalency of ligand-metal bonds. *Coord. Chem. Rev.* **2005**, *249* (1–2), 97–129.
- (30) Tenderholt, A. L.; Wang, J.-J.; Szilagyi, R. K.; Holm, R. H.; Hodgson, K. O.; Hedman, B.; Solomon, E. I. Sulfur K-Edge X-ray Absorption Spectroscopy and Density Functional Calculations on  $\text{Mo}(\text{IV})$  and  $\text{Mo}(\text{VI})=\text{O}$  Bis-dithiolenes: Insights into the Mechanism of Oxo Transfer in DMSO Reductase and Related Functional Analogues. *J. Am. Chem. Soc.* **2010**, *132* (24), 8359–8371.
- (31) Ha, Y.; Tenderholt, A. L.; Holm, R. H.; Hedman, B.; Hodgson, K. O.; Solomon, E. I. Sulfur K-Edge X-ray Absorption Spectroscopy and Density Functional Theory Calculations on Monooxo  $\text{Mo-IV}$  and Bisoxo  $\text{Mo-VI}$  Bis-dithiolenes: Insights into the Mechanism of Oxo Transfer in Sulfite Oxidase and Its Relation to the Mechanism of DMSO Reductase. *J. Am. Chem. Soc.* **2014**, *136* (25), 9094–9105.
- (32) Ha, Y.; Arnold, A. R.; Nuñez, N. N.; Bartels, P. L.; Zhou, A.; David, S. S.; Barton, J. K.; Hedman, B.; Hodgson, K. O.; Solomon, E. I. Sulfur K-Edge XAS Studies of the Effect of DNA Binding on the  $[\text{Fe}_4\text{S}_4]$  Site in EndoIII and MutY. *J. Am. Chem. Soc.* **2017**, *139* (33), 11434–11442.
- (33) Kozimor, S. A.; Yang, P.; Batista, E. R.; Boland, K. S.; Burns, C. J.; Christensen, C. N.; Clark, D. L.; Conradson, S. D.; Hay, P. J.; Lezama, J. S.; Martin, R. L.; Schwarz, D. E.; Wilkerson, M. P.; Wolfsberg, L. E. Covalency trends in group IV metallocene dichlorides. Chlorine K-edge X-ray absorption spectroscopy and time dependent-density functional theory. *Inorg. Chem.* **2008**, *47* (12), 5365–5371.
- (34) Kozimor, S. A.; Yang, P.; Batista, E. R.; Boland, K. S.; Burns, C. J.; Clark, D. L.; Conradson, S. D.; Martin, R. L.; Wilkerson, M. P.; Wolfsberg, L. E. Trends in covalency for d- and f element metallocene dichlorides identified using chlorine K-edge X-ray absorption spectroscopy and time-dependent density functional theory. *J. Am. Chem. Soc.* **2009**, *131* (34), 12125–12136.
- (35) Minasian, S. G.; Keith, J. M.; Batista, E. R.; Boland, K. S.; Clark, D. L.; Conradson, S. D.; Kozimor, S. A.; Martin, R. L.; Schwarz, D. E.; Shuh, D. K.; Wagner, G. L.; Wilkerson, M. P.; Wolfsberg, L. E.; Yang, P. Determining relative f and d orbital contributions to M-Cl covalency in  $\text{MCl}_6^{2-}$  (M = Ti, Zr, Hf, U) and  $\text{UOCl}_5^-$  using Cl K-edge X-ray absorption spectroscopy and time-dependent density functional theory. *J. Am. Chem. Soc.* **2012**, *134* (12), 5586–5597.

- (36) Löble, M. W.; Keith, J. M.; Altman, A. B.; Stieber, S. C. E.; Batista, E. R.; Boland, K. S.; Conradson, S. D.; Clark, D. L.; Lezama Pacheco, J.; Kozimor, S. A.; et al. Covalency in lanthanides. An X-ray absorption spectroscopy and density functional theory study of  $\text{LnCl}_2(\text{x})$  ( $\text{x} = 3, 2$ ). *J. Am. Chem. Soc.* **2015**, *137* (7), 2506–2523.
- (37) Spencer, L. P.; Yang, P.; Minasian, S. G.; Jilek, R. E.; Batista, E. R.; Boland, K. S.; Boncella, J. M.; Conradson, S. D.; Clark, D. L.; Hayton, T. W.; Kozimor, S. A.; Martin, R. L.; MacInnes, M. M.; Olson, A. C.; Scott, B. L.; Shuh, D. K.; Wilkerson, M. P. Tetrahedral complexes of the  $\text{U}(\text{NR})_2(2+)$  ion: Synthesis, theory, and chlorine K-edge X-ray absorption spectroscopy. *J. Am. Chem. Soc.* **2013**, *135* (6), 2279–2290.
- (38) Cross, J. N.; Su, J.; Batista, E. R.; Cary, S. K.; Evans, W. J.; Kozimor, S. A.; Mocko, V.; Scott, B. L.; Stein, B. W.; Windorff, C. J.; Yang, P. Covalency in americium(III) hexachloride. *J. Am. Chem. Soc.* **2017**, *139* (25), 8667–8677.
- (39) Su, J.; Batista, E. R.; Boland, K. S.; Bone, S. E.; Bradley, J. A.; Cary, S. K.; Clark, D. L.; Conradson, S. D.; Ditter, A. S.; Kaltsoyannis, N.; Keith, J. M.; Kerridge, A.; Kozimor, S. A.; Löble, M. W.; Martin, R. L.; Minasian, S. G.; Mocko, V.; La Pierre, H. S.; Seidler, G. T.; Shuh, D. K.; Wilkerson, M. P.; Wolfsberg, L. E.; Yang, P. Energy-degeneracy-driven covalency in actinide bonding. *J. Am. Chem. Soc.* **2018**, *140* (51), 17977–17984.
- (40) Minasian, S. G.; Keith, J. M.; Batista, E. R.; Boland, K. S.; Kozimor, S. A.; Martin, R. L.; Shuh, D. K.; Tyliczszak, T.; Vernon, L. J. Carbon K-edge X-ray absorption spectroscopy and time-dependent density functional theory examination of metal-carbon bonding in metallocene dichlorides. *J. Am. Chem. Soc.* **2013**, *135* (39), 14731–14740.
- (41) Minasian, S. G.; Keith, J. M.; Batista, E. R.; Boland, K. S.; Clark, D. L.; Kozimor, S. A.; Martin, R. L.; Shuh, D. K.; Tyliczszak, T. New evidence for 5f covalency in actinocenes determined from carbon K-edge XAS and electronic structure theory. *Chemical Science* **2014**, *5* (1), 351–359.
- (42) Smiles, D. E.; Batista, E. R.; Booth, C. H.; Clark, D. L.; Keith, J. M.; Kozimor, S. A.; Martin, R. L.; Minasian, S. G.; Shuh, D. K.; Stieber, S. C. E.; Tyliczszak, T. The duality of electron localization and covalency in lanthanide and actinide metallocenes. *Chemical Science* **2020**, *11* (10), 2796–2809.
- (43) Pemmaraju, C. D.; Copping, R.; Wang, S. A.; Janousch, M.; Teat, S. J.; Tyliczszak, T.; Canning, A.; Shuh, D. K.; Prendergast, D. Bonding and charge transfer in nitrogen-donor uranyl complexes: Insights from NEXAFS spectra. *Inorg. Chem.* **2014**, *53* (21), 11415–11425.
- (44) Wen, X. D.; Löble, M. W.; Batista, E. R.; Bauer, E.; Boland, K. S.; Burrell, A. K.; Conradson, S. D.; Daly, S. R.; Kozimor, S. A.; Minasian, S. G.; Martin, R. L.; McCleskey, T. M.; Scott, B. L.; Shuh, D. K.; Tyliczszak, T. Electronic structure and O K-edge XAS spectroscopy of  $\text{UO}_2$ . *J. Electron Spectrosc. Relat. Phenom.* **2014**, *194*, 81–87.
- (45) Altman, A. B.; Pacold, J. I.; Wang, J.; Lukens, W. W.; Minasian, S. G. Evidence for 5d sigma and 5d pi covalency in lanthanide sesquioxides from oxygen K-edge X-ray absorption spectroscopy. *Dalton. Trans.* **2016**, *45* (24), 9948–9961.
- (46) Minasian, S. G.; Batista, E. R.; Booth, C. H.; Clark, D. L.; Keith, J. M.; Kozimor, S. A.; Lukens, W. W.; Martin, R. L.; Shuh, D. K.; Stieber, S. C. E.; Tyliczszak, T.; Wen, X. D. Quantitative evidence for lanthanide-oxygen orbital mixing in  $\text{CeO}_2$ ,  $\text{PrO}_2$ , and  $\text{TbO}_2$ . *J. Am. Chem. Soc.* **2017**, *139* (49), 18052–18064.
- (47) Frati, F.; Hunault, M. O. J. Y.; de Groot, F. M. F. Oxygen K-edge X-ray absorption spectra. *Chem. Rev.* **2020**, *120* (9), 4056–4110.
- (48) Agostini, G.; Giacometti, G.; Clemente, D. A.; Vicentini, M. Crystal and molecular-structure of uranyl-nitrate trimethylphosphate. *Inorg. Chim. Acta* **1982**, *62* (2), 237–240.
- (49) Burns, J. H.; Brown, G. M.; Ryan, R. R. Structure of dinitratodioxobis(triisobutyl phosphate)uranium(VI) at 139 K. *Acta Crystallogr., Sect. C: Cryst. Struct. Commun.* **1985**, *41* (OCT), 1446–1448.
- (50) John, G. H.; May, I.; Sarsfield, M. J.; Collison, D.; Helliwell, M. Dimeric uranyl complexes with bridging perchlorates. *Dalton. Trans.* **2007**, *16*, 1603–1610.
- (51) Bandoli, G.; Bortolozzo, G.; Clemente, D. A.; Croatto, U.; Panattoni, C. Crystal and molecular structure of triphenylphosphine oxide. *J. Chem. Soc. A* **1970**, *17*, 2778–2780.
- (52) Brock, C. P.; Schweizer, W. B. Internal molecular-motion of triphenylphosphine oxide - analysis of atomic displacement parameters for orthorhombic and monoclinic crystal modifications at 100-K and 150-K. *J. Am. Chem. Soc.* **1985**, *107* (24), 6964–6970.
- (53) Etter, M. C.; Baures, P. W. Triphenylphosphine oxide as a crystallization aid. *J. Am. Chem. Soc.* **1988**, *110* (2), 639–640.
- (54) Davies, J. A.; Dutremez, S.; Pinkerton, A. A. Solid-state phosphorus-31 NMR and X-ray crystallographic studies of tertiary phosphines and their derivatives. *Inorg. Chem.* **1991**, *30* (10), 2380–2387.
- (55) Alfarhan, K. A. Crystal-structure of triphenylphosphine oxide. *J. Crystallogr. Spectrosc. Res.* **1992**, *22* (6), 687–689.
- (56) Thomas, J. A.; Hamor, T. A. Structure of orthorhombic triphenylphosphine oxide - A redetermination at room-temperature. *Acta Crystallogr., Sect. C: Cryst. Struct. Commun.* **1993**, *49*, 355–357.
- (57) Orama, O.; Koskinen, J. T. Ethyldiphenylphosphine oxide,  $(\text{C}_6\text{H}_5)_2\text{C}(\text{C}_2\text{H}_5)\text{PO}$ . *Acta Crystallogr., Sect. C: Cryst. Struct. Commun.* **1994**, *50*, 608–609.
- (58) Hilliard, C. R.; Bhuvanesh, N.; Gladysz, J. A.; Bluemel, J. Synthesis, purification, and characterization of phosphine oxides and their hydrogen peroxide adducts. *Dalton. Trans.* **2012**, *41* (6), 1742–1754.
- (59) Hilliard, C. R.; Kharel, S.; Cluff, K. J.; Bhuvanesh, N.; Gladysz, J. A.; Bluemel, J. Structures and Unexpected Dynamic Properties of Phosphine Oxides Adsorbed on Silica Surfaces. *Chem. - Eur. J.* **2014**, *20* (52), 17292–17295.
- (60) Donahue, C. M.; McCollom, S. P.; Forrest, C. M.; Blake, A. V.; Bellott, B. J.; Keith, J. M.; Daly, S. R. Impact of Coordination Geometry, Bite Angle, and Trans Influence on Metal-Ligand Covalency in Phenyl-Substituted Phosphine Complexes of Ni and Pd. *Inorg. Chem.* **2015**, *54* (12), 5646–5659.
- (61) Lee, K.; Wei, H.; Blake, A. V.; Donahue, C. M.; Keith, J. M.; Daly, S. R. Ligand K-edge XAS, DFT, and TDDFT analysis of pincer linker variations in Rh(I) PNP complexes: reactivity insights from electronic structure. *Dalton. Trans.* **2016**, *45* (24), 9774–9785.
- (62) Donahue, C. M.; Daly, S. R. Ligand K-Edge XAS Studies of Metal-Phosphorus Bonds: Applications, Limitations, and Opportunities. *Comments Inorg. Chem.* **2018**, *38* (2), 54–78.
- (63) Lee, K.; Blake, A. V.; Donahue, C. M.; Spielvogel, K. D.; Bellott, B. J.; Daly, S. R. Quantifying the Interdependence of Metal-Ligand Covalency and Bond Distance using Ligand K-edge XAS. *Angew. Chem., Int. Ed.* **2019**, *58*, 12451–12455.
- (64) Lee, K.; Wei, H.; Blake, A. V.; Donahue, C. M.; Keith, J. M.; Daly, S. R. Measurement of Diphosphine sigma-Donor and pi-Acceptor Properties in d(0) Titanium Complexes Using Ligand K-Edge XAS and TDDFT. *Inorg. Chem.* **2018**, *57* (16), 10277–10286.
- (65) Blake, A. V.; Wei, H. C.; Lee, K.; Donahue, C. M.; Keith, J. M.; Daly, S. R. Solution and Solid-State Ligand K-Edge XAS Studies of  $\text{PdCl}_2$  Diphosphine Complexes with Phenyl and Cyclohexyl Substituents. *Eur. J. Inorg. Chem.* **2018**, *2018* (20–21), 2267–2276.
- (66) Fortier, S.; Hayton, T. W. Oxo ligand functionalization in the uranyl ion ( $\text{UO}_2^{2+}$ ). *Coord. Chem. Rev.* **2010**, *254* (3–4), 197–214.
- (67) Fillaux, C.; Guillaumont, D.; Berthet, J.-C.; Copping, R.; Shuh, D. K.; Tyliczszak, T.; Auwer, C. D. Investigating the electronic structure and bonding in uranyl compounds by combining NEXAFS spectroscopy and quantum chemistry. *Phys. Chem. Chem. Phys.* **2010**, *12* (42), 14253–14262.
- (68) Martin, R. L.; Shirley, D. A. Many electron theory of electron emission. In *Electron Spectroscopy: Theory, Techniques and Applications*; Brundle, C. R., Baker, A. D., Eds.; Academic Press: London, 1977; Vol. 1, pp 75–117.
- (69) Segala, M.; Chong, D. P. K-shell core-electron binding energies for phosphorus- and sulfur-containing molecules calculated by density

- functional theory. *J. Electron Spectrosc. Relat. Phenom.* **2010**, *182* (3), 141–144.
- (70) Barton, R. L.; Gardenghi, D. J.; Stolte, W. C.; Szilagy, R. K. Multiedge X-ray absorption spectroscopy Part II: XANES analysis of bridging and terminal chlorides in hexachlorodipalladate(II) complex. *J. Phys. Chem. A* **2015**, *119* (22), 5579–5586.
- (71) McLaughlin, B. M.; Ballance, C. P.; Bowen, K. P.; Gardenghi, D. J.; Stolte, W. C. High precision k-shell photoabsorption cross sections for atomic oxygen: Experiment and theory. *Astrophys. J., Lett.* **2013**, *779* (2), L31.
- (72) Stöhr, J. *NEXAFS Spectroscopy*. Springer-Verlag: Berlin, 1992.
- (73) Groot, F. d.; Kotani, A. *Core Level Spectroscopy of Solids*; CRC Press, 2008.
- (74) Neese, F.; Hedman, B.; Hodgson, K. O.; Solomon, E. I. Relationship between the dipole strength of ligand pre-edge transitions and metal-ligand covalency. *Inorg. Chem.* **1999**, *38* (21), 4854–4860.
- (75) de Sahb, C.; Watson, L. A.; Nadas, J.; Hay, B. P. Design Criteria for Polyazine Extractants To Separate AnIII from LnIII. *Inorg. Chem.* **2013**, *52* (18), 10632–10642.
- (76) Pham, T. A.; Altman, A. B.; Stieber, S. C. E.; Booth, C. H.; Kozimor, S. A.; Lukens, W. W.; Olive, D. T.; Tyliczszak, T.; Wang, J.; Minasian, S. G.; Raymond, K. N. A Macrocyclic Chelator That Selectively Binds Ln4+ over Ln3+ by a Factor of 1029. *Inorg. Chem.* **2016**, *55* (20), 9989–10002.
- (77) Hudson, M. J.; Harwood, L. M.; Laventine, D. M.; Lewis, F. W. Use of Soft Heterocyclic N-Donor Ligands To Separate Actinides and Lanthanides. *Inorg. Chem.* **2013**, *52* (7), 3414–3428.
- (78) Manna, D.; Ghanty, T. K. Complexation behavior of trivalent actinides and lanthanides with 1,10-phenanthroline-2,9-dicarboxylic acid based ligands: insight from density functional theory. *Phys. Chem. Chem. Phys.* **2012**, *14* (31), 11060–11069.
- (79) Roy, L. E.; Bridges, N. J.; Martin, L. R. Theoretical insights into covalency driven f element separations. *Dalton. Trans.* **2013**, *42* (7), 2636–2642.
- (80) Xiao, C.-L.; Wang, C.-Z.; Yuan, L.-Y.; Li, B.; He, H.; Wang, S.; Zhao, Y.-L.; Chai, Z.-F.; Shi, W.-Q. Excellent Selectivity for Actinides with a Tetradentate 2,9-Diamide-1,10-Phenanthroline Ligand in Highly Acidic Solution: A Hard-Soft Donor Combined Strategy. *Inorg. Chem.* **2014**, *53* (3), 1712–1720.
- (81) Xiao, C.-L.; Wu, Q.-Y.; Wang, C.-Z.; Zhao, Y.-L.; Chai, Z.-F.; Shi, W.-Q. Quantum Chemistry Study of Uranium(VI), Neptunium(V), and Plutonium(IV,VI) Complexes with Preorganized Tetradentate Phenanthrolineamide Ligands. *Inorg. Chem.* **2014**, *53* (20), 10846–10853.
- (82) Surbella, R. G., III; Andrews, M. B.; Cahill, C. L. Self assembly of  $\text{UO}_2 \times 4(2-)$  ( $X = \text{Cl}, \text{Br}$ ) dianions with gamma substituted pyridinium cations: Structural systematics and fluorescence properties. *J. Solid State Chem.* **2016**, *236*, 257–271.
- (83) Crawford, M. J.; Mayer, P. Synthesis, structural and computational investigations of  $\text{UO}_2\text{I}_4^{2-}$ : A structurally characterized U(VI)-I anion. *Inorg. Chem.* **2005**, *44* (16), 5547–5549.
- (84) Sheldrick, G. M. A short history of SHELX. *Acta Crystallogr., Sect. A: Found. Crystallogr.* **2008**, *64*, 112–122.
- (85) Dolomanov, O. V.; Bourhis, L. J.; Gildea, R. J.; Howard, J. A. K.; Puschmann, H. OLEX2: a complete structure solution, refinement and analysis program. *J. Appl. Crystallogr.* **2009**, *42*, 339–341.
- (86) Ren, G. X.; Zhang, N.; Feng, X. F.; Zhang, H.; Yu, P. F.; Zheng, S.; Zhou, D.; Tian, Z. W.; Liu, X. S. Photon-in/photon-out endstation for studies of energy materials at beamline 02B02 of Shanghai Synchrotron Radiation Facility. *Chin. Phys. B* **2020**, *29* (1), No. 016101.
- (87) Zheng, L.; Zhao, Y. D.; Tang, K.; Ma, C. Y.; Hong, C. H.; Han, Y.; Cui, M. Q.; Guo, Z. Y. A new experiment station on beamline 4B7A at Beijing Synchrotron Radiation Facility. *Spectrochim. Acta, Part B* **2014**, *101*, 1–5.
- (88) Ravel, B.; Newville, M. ATHENA, ARTEMIS, HEPHAESTUS: data analysis for X-ray absorption spectroscopy using IFEFFIT. *J. Synchrotron Radiat.* **2005**, *12*, 537–541.
- (89) George, G. N. *EDG FIT*; Stanford Synchrotron Radiation Laboratory, Stanford Linear Accelerator Center, Stanford University: Stanford, CA, 2001.
- (90) Baerends, E. J.; Ziegler, T.; Autschbach, J.; Bashford, D.; Bérces, A.; Bickelhaupt, F. M.; Bo, C.; Boerrigter, P. M.; Cavallo, L.; Chong, D. P. et al. *ADF2019*; SCM, Theoretical Chemistry, Vrije Universiteit, Amsterdam, The Netherlands, 2019. <https://www.scm.com/product/adf/>.
- (91) te Velde, G.; Bickelhaupt, F. M.; Baerends, E. J.; Fonseca Guerra, C.; van Gisbergen, S. J. A.; Snijders, J. G.; Ziegler, T. Chemistry with ADF. *J. Comput. Chem.* **2001**, *22* (9), 931–967.
- (92) Becke, A. D. Density-functional exchange-energy approximation with correct asymptotic-behavior. *Phys. Rev. A: At., Mol., Opt. Phys.* **1988**, *38* (6), 3098–3100.
- (93) Lee, C. T.; Yang, W. T.; Parr, R. G. Development of the Colle-Salvetti correlation-energy formula into a functional of the electron-density. *Phys. Rev. B: Condens. Matter Mater. Phys.* **1988**, *37* (2), 785–789.
- (94) Faas, S.; Snijders, J. G.; Vanlenthe, J. H.; Vanlenthe, E.; Baerends, E. J. The ZORA formalism applied to the Dirac-Fock equation. *Chem. Phys. Lett.* **1995**, *246* (6), 632–640.
- (95) Grimme, S. A simplified Tamm-Dancoff density functional approach for the electronic excitation spectra of very large molecules. *J. Chem. Phys.* **2013**, *138* (24), 244104.
- (96) Bannwarth, C.; Grimme, S. A simplified time-dependent density functional theory approach for electronic ultraviolet and circular dichroism spectra of very large molecules. *Comput. Theor. Chem.* **2014**, *1040*, 45–53.